



# The emerging role of photoacoustic imaging in clinical oncology

Li Lin<sup>1</sup> and Lihong V. Wang<sup>1,2</sup>✉

**Abstract** | Clinical oncology can benefit substantially from imaging technologies that reveal physiological characteristics with multiscale observations. Complementing conventional imaging modalities, photoacoustic imaging (PAI) offers rapid imaging (for example, cross-sectional imaging in real time or whole-breast scanning in 10–15 s), scalably high levels of spatial resolution, safe operation and adaptable configurations. Most importantly, this novel imaging modality provides informative optical contrast that reveals details on anatomical, functional, molecular and histological features. In this Review, we describe the current state of development of PAI and the emerging roles of this technology in cancer screening, diagnosis and therapy. We comment on the performance of cutting-edge photoacoustic platforms, and discuss their clinical applications and utility in various clinical studies. Notably, the clinical translation of PAI is accelerating in the areas of macroscopic and mesoscopic imaging for patients with breast or skin cancers, as well as in microscopic imaging for histopathology. We also highlight the potential of future developments in technological capabilities and their clinical implications, which we anticipate will lead to PAI becoming a desirable and widely used imaging modality in oncological research and practice.

Photoacoustic imaging (PAI), also known as optoacoustic imaging, is an emerging modality that has generated increasing interest for its uses in clinical research and translation, including early promise for the management of patients with cancer. As a hybrid technique, PAI combines the advantages of optical excitation with those of acoustic detection in a modality that complements conventional technologies. Specifically, the optical excitation provides rich contrasts that reveal a level of anatomical, functional and molecular information (such as detailed vascular structures<sup>1,2</sup>, haemoglobin oxygen saturation<sup>3</sup>, and uptake of contrast agents<sup>4</sup>). At the same time, acoustic detection benefits from the limited scattering of ultrasound waves in biological tissues, enabling PAI to generate high-resolution images with the desired depth ( $\leq 4$  cm in human breasts that are compressed against the chest wall<sup>1,5</sup>). This distinctive feature is enabled by the photoacoustic effect, in which absorbed photons are converted into propagating acoustic waves. When short pulses of light are used to irradiate biological tissues, photon absorption by the tissue thermoelastically induces a transient pressure increase, which propagates as ultrasonic waves (referred to as photoacoustic waves). The photoacoustic waves are then detected by ultrasonic transducers and can then be used to reconstruct the optical absorption distribution in the tissue<sup>6</sup>.

Over the past two decades, PAI has enabled various exciting discoveries and applications, from preclinical research to clinical care<sup>6–11</sup>. In preclinical studies, PAI has become an irreplaceable tool, providing high-speed *in vivo* imaging with informative optical contrast, a high level of spatial resolution and whole-body penetration in small animals<sup>12,13</sup>. Translational PAI has also attracted growing interest in oncology<sup>11</sup>, dermatology<sup>14</sup>, paediatrics<sup>15</sup>, neuroscience<sup>16</sup> and orthopaedics<sup>17</sup>, among other areas of study<sup>7</sup>. Specifically, PAI has demonstrated a complementary role in cancer imaging (TABLE 1; BOXES 1,2), thus enabling improved screening, diagnosis, and treatment of patients with cancer<sup>18–21</sup>.

The unique physical characteristics of PAI enable the investigator to image the anatomy, function and molecular processes of biological systems *in vivo* owing to differences in the optical absorption spectra of a wide range of endogenous and/or exogenous contents<sup>22</sup>. Accordingly, multicontrast PAI can provide comprehensive information that can assist in cancer imaging without the need for ionizing radiation, heavy-metal contrast agents, or specific facilities for radiation shielding. In addition to the advantages provided by optical absorption contrast, its combination with ultrasound detection endows PAI with many of the advantages of clinical ultrasonography: a convenient system geometry (provided by an open imaging platform) and a scalable

<sup>1</sup>Caltech Optical Imaging Laboratory, Andrew and Peggy Cherng Department of Medical Engineering, California Institute of Technology, Pasadena, CA, USA.

<sup>2</sup>Department of Electrical Engineering, California Institute of Technology, Pasadena, CA, USA.

✉e-mail: LVW@caltech.edu

<https://doi.org/10.1038/s41571-022-00615-3>

### Key points

- Photoacoustic imaging (PAI) has emerged as an appealing modality that can complement existing imaging techniques for cancer screening, diagnosis and treatment guidance.
- The elegant fusion of light and sound provides PAI with several distinctive capabilities including scalable spatial resolution and imaging depth while maintaining a high imaging speed.
- By selecting suitable optical wavelengths, PAI can image a wide variety of endogenous molecules or exogenous agents, revealing the anatomy, histology, function and molecular activity of biological systems *in vivo*.
- Taking advantage of the high sensitivity to tumour-associated hypoxia and angiogenesis, PAI has the potential to enable early detection of cancers of the breast, skin and prostate.
- The role of PAI in clinical oncology has been demonstrated by the first FDA approval of this technology for breast cancer diagnosis; other areas of potential clinical application include cancer detection, biopsy guidance and molecular imaging.
- In addition to cancer screening and diagnosis, PAI has shown potential benefit for the assessment of responses to neoadjuvant chemotherapy, guiding surgical resection and monitoring drug delivery.

high level of spatial resolution. The rapid imaging speed and operational safety further enhance the suitability of PAI for frequent and repeated bedside imaging. Working in different configurations, the scale of PAI imaging can vary from organs to organelles<sup>23</sup>, and this approach has been applied for imaging of breast cancer<sup>5,24,25</sup>, skin cancer<sup>26,27</sup>, prostate cancer<sup>4</sup>, metastatic lymph nodes<sup>28</sup> and circulating cancer cell clusters<sup>29</sup>, as well as for microscopy of excised tumour samples<sup>30</sup>. With these capabilities, PAI is rapidly evolving into a medically translatable modality. In 2021, one of the many companies working on PAI received FDA approval for a combined PAI and ultrasonography imaging system<sup>31</sup>, thus paving the way for further clinical translation.

In this Review, we describe the progress of PAI towards clinical translation, highlighting selected notable outcomes from various oncological applications, and envision the future role of this emerging technology (BOXES 3,4). We first introduce the major configurations of PAI that enable scalability with rapid image acquisition. We then consider the contrast mechanisms of PAI and how these reveal anatomical, histological, functional and molecular details that cannot be easily detected or clearly imaged using other modalities. To illustrate these imaging capabilities, we describe representative PAI studies involving patients with cancer, and divide the roles of PAI into cancer detection, diagnosis and treatment guidance. We conclude with a summary of the state-of-the-art and provide perspectives on possible future technical breakthroughs and their clinical implications.

### Multiscale PAI

PAI has been developed into several configurations, providing multiscale imaging of physiological characteristics<sup>10</sup>. A substantial majority of PAI modalities are safe for use in humans because the level of radiation exposure or optical fluence (energy per unit area) on the skin surface is usually well within the American National Standards Institute (ANSI) safety limit<sup>32</sup>. These limits include a maximum permissible skin exposure to

1,064 nm light of 100 mJ/cm<sup>2</sup> for each nanosecond laser pulse and 1 W/cm<sup>2</sup> for exposure durations exceeding 10 s.

### Major PAI modalities

PAI is typically implemented as one of three major modalities: photoacoustic microscopy (PAM); photoacoustic CT (PACT); or photoacoustic endoscopy (PAE) (FIG. 1a). In PAM<sup>33</sup>, volumetric imaging is conducted using two-dimensional raster scanning of the dual foci of optical excitation and ultrasonic detection (FIG. 1b). At each scanning position, the ultrasonic transducer receives photoacoustic signals along the line excited by the laser light, recording the acoustic time-of-arrival and producing a one-dimensional image along the depth direction. PACT<sup>22</sup>, however, uses an expanded laser beam to illuminate the biological tissue and an ultrasonic transducer array to concurrently detect photoacoustic waves from multiple angles (FIG. 1c). Image reconstruction — essentially the sophisticated triangulation of optical absorbers from the time-resolved ultrasonic signals — is used to reconstruct PACT images<sup>34</sup>. Evolved from PAM and PACT, PAE<sup>35</sup> is an adaptation of these modalities designed to fit into an endoscope that can be used for imaging internal organs.

### Scalable high-speed imaging

PAM generally provides microscopic and mesoscopic resolution at a millimetre-level imaging depth (FIG. 1d,e), whereas PACT enables tissue imaging to depths of several centimetres at mesoscopic and macroscopic levels of resolution (FIG. 1f). Compared to PAM, PACT usually provides deeper tissue penetration, a larger field of view (FOV), and a faster imaging speed, albeit at the expense of higher system and computational costs.

Depending on whether the optical or acoustic focus is finer, PAM can be further classified into optical resolution (OR) and acoustic resolution (AR) PAM. In OR-PAM, the optical focus laterally confines the photoacoustic excitation at micrometre scale, with an imaging depth that is limited by optical diffusion to 1 mm *in vivo* (FIG. 1d). To image at depths of >1 mm, AR-PAM relies on acoustic focusing to laterally confine the photoacoustic detection to tens of micrometres, with a depth up to a few millimetres (FIG. 1e), which is mainly limited by the frequency-dependent acoustic attenuation. Using lower ultrasound frequencies for detection, PACT is less affected by acoustic attenuation but provides coarser levels of resolution than PAM. Largely limited by light attenuation<sup>10,36</sup>, PACT usually enables imaging depths of up to a few centimetres with a resolution of hundreds of micrometres (FIG. 1f). The typical ratio of imaging depth to spatial resolution across the different PAI configurations is >100, making PAI a high-resolution modality across broad length scales<sup>23</sup>. The optimal trade-off between spatial resolution and imaging depth depends on the application.

Equipped with a pulsed laser with a high repetition rate and with a fast scanner (such as a galvo mirror) steering the optical and acoustic beams, modern high-speed OR-PAM systems can achieve frame rates of over a few hertz when imaging millimetre-scale 3D regions<sup>37,38</sup>. High-speed PAM enables the imaging of dynamic

phenomena such as blood flow redistribution in mouse models of non-fatal stroke at microscopic scales<sup>39</sup>; this approach can also be miniaturized for hand-held devices<sup>40,41</sup> for human skin imaging. PACT has been used for real-time 2D and 3D imaging using parallel acoustic detection. In covering a larger FOV (such as an entire human breast), PACT can perform a complete scan within the limits of a single breath-hold of 10–15 s<sup>1,5</sup>. PACT has been used to monitor functional activation of the brain during motor function and language tasks in patients who have had a hemispherectomy<sup>42</sup>.

**Contrast mechanisms**

Owing to the fact that each basic biological component of an image has a distinct optical absorption spectrum (FIG. 2a), PAI enables the distribution of a wide variety of endogenous or exogenous chromophores to be mapped in vivo by rapidly tuning the excitation light to multiple wavelengths. Haemoglobin, myoglobin, melanin, water, lipids and nucleic acids can all be imaged endogenously in this way. The use of exogenous contrast agents, such as nanoparticles and organic dyes<sup>43,44</sup>, extends PAI into the domain of molecular imaging.

**Anatomical and histological contrast**

Among the chemical components of most tissues, haemoglobin is one of the major absorbers in the visible and short-wavelength near-infrared (NIR) spectra<sup>45</sup>. Accordingly, PAI is naturally suited to delineating angiographic anatomy (FIG. 2b) without the need for ionizing radiation or injected contrast agents, and has a high level of sensitivity for imaging small vasculatures (for example, capillaries of the skin<sup>2</sup> or arterioles of the breast<sup>1,5</sup>). Angiogenesis, which has a central role in cancer development, invasion and metastasis<sup>46,47</sup>, and is thus a hallmark of cancer<sup>48</sup>, can be detected and characterized using PAI. Furthermore, PAI enables spectral differentiation between other molecules, including water, lipids, proteins<sup>3,49</sup> (FIGS 1d,2c) and melanin<sup>50</sup>. Capitalizing on

the strong ultraviolet absorption properties of nucleic acids (such as DNA and RNA), PAM has been used to image the nuclei of individual cells without staining, thus providing a label-free alternative to traditional ex vivo histological staining methods<sup>30</sup> (FIG. 2d).

**Functional and molecular contrast**

In addition to anatomical structures, spectroscopic PAI enables the characterization of functional and molecular features, thus more comprehensively reflecting the underlying physiological and pathological conditions. Functional imaging usually reveals physiological activity at the organ or tissue level, while molecular imaging typically captures biological and pathophysiological processes at the molecular level<sup>51</sup>. Functional imaging generally measures endogenous contrast, whereas molecular imaging uses exogenous contrast to label biomarkers in vivo. Here, we divide the functional contrast of PAI into haemoglobin oxygen saturation (sO<sub>2</sub>) and dynamic information, and categorize the molecular contrast agents into nanoparticles and organic dyes.

**Haemoglobin oxygen saturation.** As a primary oxygen carrier, haemoglobin is essential to tissue metabolism. By separating the individual contributions of oxyhaemoglobin (HbO<sub>2</sub>) and deoxyhaemoglobin (HbR), the total concentration (HbT) and extent of sO<sub>2</sub> can be assessed<sup>45</sup> (FIG. 2b,c). These two factors are the most commonly used indices of blood perfusion and oxygenation, respectively. sO<sub>2</sub> might not be uniquely correlated with the partial pressure of oxygen<sup>52</sup>, although sO<sub>2</sub> maps have shown a good correlation with cellular markers of hypoxia<sup>45</sup>. Compared with other sO<sub>2</sub> measurement modalities, which are typically based on diffuse optics<sup>53</sup>, PAI provides higher spatial resolution in the optical diffusive regime<sup>23</sup>.

**Dynamic contrast.** Owing to the rapid imaging speed, PAI can record haemodynamics<sup>1,37</sup>, tissue deformation<sup>5,12</sup> and provide data on thermodynamics (such as

Table 1 | Comparison of PAI with established breast imaging modalities

Properties	CE MRI	Ultrasonography	Mammography	PET	PAI
Contrast	Vascular contrast agent	Acoustic scattering	Atomic number	Radioactive tracer	Optical absorption
Functional imaging of breast cancer	Yes	No	No	Yes	Yes
Spatial resolution	Good (≥0.45 mm) <sup>209,210</sup>	Good (>0.20 mm) <sup>211</sup>	Excellent (≥0.05 mm) <sup>212,213</sup>	Poor (≥6.1 mm) <sup>214</sup>	Good (≥0.26 mm) <sup>5</sup>
Imaging depth	Excellent (whole body)	Good (2–8 cm) <sup>211,215</sup>	Good (5–7 cm) <sup>216</sup>	Excellent (whole body)	Good (4–5 cm) <sup>1,5,217</sup>
Imaging speed <sup>a</sup>	Low (9–40 min) <sup>218,219</sup>	Moderate (3–13 min) <sup>101,220</sup>	Moderate (3–4 min) <sup>221</sup>	Moderate (3–10 min) <sup>222,223</sup>	High (≤30 s) <sup>1,5</sup>
Involves ionizing radiation	No	No	Yes	Yes	No
Requires exogenous agents	Yes	No	No	Yes	No
Availability/repeatability <sup>b</sup>	Low	High	Low	Low	High
Bedside imaging	No	Yes	No	No	Yes

CE MRI, contrast-enhanced MRI; PAI, photoacoustic imaging. <sup>a</sup>Imaging speed is considered for whole-breast imaging, with patient positioning time excluded. <sup>b</sup>Availability/repeatability are evaluated by considering the use of ionizing radiation or exogenous contrast agent and the time/financial cost.

**Box 1 | Advantages of photoacoustic imaging**

After years of maturation<sup>225</sup>, photoacoustic imaging (PAI) is currently being translated into clinical applications, with various studies currently underway. From the technical perspective, PAI offers the following advantages as a complement to conventional imaging modalities. These distinct advantages and compatibilities enable PAI to be combined with other imaging technologies for multimodality and multicontrast imaging that provide more comprehensive levels of information.

**Complementing pure optical imaging modalities**

PAI breaks through the current fundamental depth limits of optical microscopy while maintaining a high level of spatial resolution in deep tissue. A depth to resolution ratio of >100 is usually guaranteed with PAI-based imaging. For example, photoacoustic microscopy can provide micrometre-level resolution with millimetre-level imaging depth. In photoacoustic CT, the spatial resolution can be scaled up to hundreds of micrometres with centimetre-level imaging depth.

**Complementing ultrasonography**

PAI is highly sensitive to optical absorption, enabling anatomical, functional and molecular imaging based on physiologically-specific endogenous and exogenous contrasts. Because blood vessels provide acoustically smooth optical absorption boundaries, the speckling artefacts associated with ultrasonography are largely suppressed in photoacoustic images<sup>226</sup>.

**Complementing MRI and PET**

PAI can provide high-speed and high-resolution imaging without the need for heavy-metal-based or radioactive contrast agents. PAI also has an open platform and does not require radiation shielding. PAI can be variously implemented as a bedside scanner or a hand-held probe, or via an endoscope, among other configurations.

**Complementing X-ray modalities**

PAI involves non-ionizing radiation, and therefore carries fewer safety risks than X-ray modalities, thus enabling more-frequent use and closer monitoring. In human breast imaging, PAI is not strongly affected by breast density and does not require painful craniocaudal or mediolateral compression.

temperature variations)<sup>54</sup> mostly in real time. For example, when monitoring the tissue deformation induced by breathing, PACT has been successfully used to determine differences in compliance between malignant and surrounding non-malignant tissues, thus providing an alternative and concurrent contrast-based method of detecting cancer<sup>5</sup>. By imaging both static and dynamic contrast, PAI has the potential to image differences in metabolic activity. For example, by measuring vessel diameter, HbT, sO<sub>2</sub>, the tissue volume of interest and blood flow velocity, PAI enables the metabolism of oxygen (MRO<sub>2</sub>) to be measured in vivo<sup>55,56</sup>.

**Nanoparticles and organic dyes.** Nanoparticles can be engineered for a desired absorption spectrum, and their bioconjugation enables biomarkers to be targeted during both molecular imaging and drug delivery<sup>57,58</sup>. Organic dyes can be cleared from the body rapidly owing to their small molecular size, and many have been approved for clinical use. For example, changes in tumour vascular permeability can be assessed by imaging the leakage of indocyanine green (ICG)<sup>59</sup>. Exogenous contrast agents can also be useful in imaging structures with limited optical absorption at specific wavelengths (such as lymph nodes)<sup>60</sup> and in labelling pathological phenomena.

**Combining with other imaging modalities**

Combining PAI with information from other established imaging modalities (such as ultrasonography and MRI) facilitates more informative clinical imaging. Sharing the

same acoustic detection and data acquisition systems, the combination of an ultrasound scanner with the optical transmitting elements required for PAI essentially results in a combined ultrasonography and PACT device. The anatomical, functional and molecular contrast provided by PACT can then be naturally coregistered to the ultrasound images<sup>61</sup> (FIG. 2e). Apart from the incorporation of ultrasonography, PACT can also be combined with other imaging modalities. For example, in a fused MRI and photoacoustic image (FIG. 2f), centripetal blood vessels are visible towards the middle of the tumour, demonstrating the presence of two contrast mechanisms in a single image<sup>62</sup>. PACT has also been integrated with fluorescence tomography for simultaneous acquisition of optical absorption and fluorescent or bioluminescent signals<sup>63</sup>. In addition to PACT, PAM has been combined with optical coherence tomography<sup>64,65</sup>, and two-photon<sup>66</sup> and confocal microscopy<sup>67</sup> to add imaging contrast such as optical scattering and fluorescence.

**Cancer detection**

Most tumours do not produce substantial morphological changes during the early stages of development. Therefore, physiological information is critical for the accurate early detection of cancer<sup>68,69</sup>. Taking advantage of the high sensitivity of PAI for tumour-associated hypoxia<sup>70,71</sup> and angiogenesis, early cancer detection is currently one of the most promising applications of PAI and is currently approaching clinical translation. For the purposes of this discussion, we group studies using PAI for cancer detection into four categories: breast cancer screening, skin cancer imaging, prostate cancer detection and preliminary studies of other cancers.

**Breast cancer screening**

Breast cancer is the most commonly diagnosed cancer and the second leading cause of cancer death among women in the USA. Early detection of breast cancer enables improved patient management and survival. An ideal breast cancer screening modality enables cancer detection with high levels of sensitivity and specificity, a low risk of adverse events, a low level of operator dependency, fast acquisition speed and low operational costs. Currently, all FDA-approved imaging technologies can only partially fulfil these criteria, providing complementary information and advantages based on different methods of cancer detection. For example, mammography is extensively used for breast cancer screening, although this technique has reduced sensitivity in women with dense breasts (24–47% in women with heterogeneous dense breasts compared with 71–78% in women with fatty breasts<sup>72,73</sup>) and requires ionizing radiation, thus increasing the risk to benefit ratio<sup>74</sup>. Ultrasonography has been used as an adjunct to mammography-based screening, although considerable room for improvement exists, considering the low level of specificity (65–89%)<sup>73,75</sup>, operator dependency and the potential for speckle artefacts.

Like most solid tumours, breast cancers require the formation of new blood vessels (via neovascularization or angiogenesis) if they are to grow beyond a few millimetres in diameter<sup>76–78</sup>. An abundance of clinical

evidence indicates that angiogenesis clearly begins at the breast carcinoma in situ stage or earlier<sup>79–85</sup>. Evidence also indicates an increase in blood vessel density in the pathogenesis of simple breast hyperplasia<sup>86,87</sup>. In addition to the increased density and an irregular morphology<sup>88,89</sup>, these newly formed vessels usually have increased permeability, which enables delineation of the tumour based on the extravasation of gadolinium (or ICG), which can be detected using contrast-enhanced MRI (CE MRI) (or PACT<sup>59</sup>). Nonetheless, the angiogenesis, as well as its underlying stimulus, local hypoxia<sup>76,90</sup>, can act as natural sources of imaging contrast for PACT regardless of breast density, thus introducing additional physiological information to current breast screening methodologies. From the engineering perspective, a well-designed breast PACT system should have optimized configurations for optical illumination and acoustic detection. Specifically, the most widely used acoustic detection configurations include linear, planar, cylindrical and hemispherical matrices<sup>91</sup> (Supplementary Information), as discussed below:

1. Linear and planar detection. Linear ultrasonic arrays, which are used in many commercially available ultrasonography systems, have been widely adopted for

breast PACT. To enlarge the FOV, researchers have scanned the linear array to translate the imaging plane along the orthogonal dimension, thus allowing 3D imaging<sup>92,93</sup>. Heijblom et al. also describe the development of a photoacoustic mammoscope using a flat 588-element ultrasonic array to provide a larger FOV<sup>94</sup>.

2. Cylindrical detection (FIG. 3a). A cylindrical detection matrix is usually achieved by elevational scanning of a circular array designed to accommodate cylindrical objects and provide panoramic detection within the FOV. The merits of cylindrical photoacoustic detection are demonstrated by single-breath-hold breast PACT<sup>5</sup>, which can be used for both 2D imaging of breast cross-sections and 3D imaging of the whole breast by scanning a circular array within a single breath-hold of 15 s. In a pilot study, this PACT system clearly identified eight of nine breast tumours via delineation of the angiographic anatomy (FIG. 3a). Taking advantage of the high imaging speed, PACT was able to detect stiffer tumours by assessing differences in tissue deformation caused by breathing<sup>5</sup> (FIG. 3b), which enabled the detection of the tumour that was originally missed by angiographic imaging. Owing to the high level of spatiotemporal resolution, PACT systems can differentiate arteries from veins by detecting blood flow-mediated arterial deformations at a speed that is sufficient to capture the deformations induced by individual heart beats. In this system, real-time 2D imaging was achieved by compromising the elevational resolution (5.6 mm) in the 3D imaging mode<sup>5</sup>.
3. Hemispherical detection: Rotational scanning of an arc-shaped or hemispherical array has been implemented for partial spherical view coverage and dense sampling, providing 3D isotropic resolution<sup>1,62,95–97</sup>. As an example, a PACT breast imaging system cooperatively developed by Kyoto University and Canon provides elegant breast images with isotropic 3D spatial resolution, albeit at a relatively low imaging speed (2 min)<sup>97</sup>. This prototype used broadband ultrasonic transducers for PACT and a linear array for ultrasonography, thus providing co-registered images in the same coordinates. This system also enables the imaging of tumour-related blood vessels and assessments of blood oxygenation levels (FIG. 2b). However, the well-resolved FOV (a small spherical region, in the absence of scanning<sup>98</sup>) of the detector array recovered the breast volume only near the skin surface owing to a lack of elevational scanning. To overcome this limitation, another hemispherical PACT system was developed, which rotates four arc-shaped ultrasonic arrays, each of which features 256 transducer elements (FIG. 1c), enabling a greater density of spatial sampling in the elevational planes, thus providing images of similarly high quality with both deeper tissue penetration (4 cm in human breasts) and higher imaging speed (10 s)<sup>1</sup> (FIG. 1f).

Each representative prototype classified into the three detection configurations has certain advantages and limitations. The optimal configuration depends on the specific application, which requires certain levels of

## Box 2 | Current challenges of PAI

As with any imaging technology, photoacoustic imaging (PAI) has certain limitations, three of which we discuss here:

### Optical penetration

Optical attenuation of the excitation light typically limits the imaging depth of PAI to 4–5 cm in biological tissues<sup>1,22</sup>. The imaging depth can be further increased using lasers with higher levels of pulse energy or ultrasonic detectors with improved sensitivity. Attempting to improve the performance of PAI technologies within the optical dissipation limit<sup>10</sup>, which is already adequate for many applications, is likely to be a more productive use of resources. Nonetheless, microwave-induced thermoacoustic tomography (TAT), a microwave analogue of photoacoustic CT, provides a possible method of overcoming the depth limit. Instead of using light for excitation, TAT uses microwaves, generating heat through both dielectric relaxation of water molecules and ionic conductivity. Therefore, TAT can reveal differences in the water and ionic content of biological tissues with deeper tissue penetration<sup>227–230</sup>. For example, the penetration depth (at which radiation intensity falls to 37% of its value at the surface) of 1-GHz microwaves in fat is around 8 cm<sup>231</sup>.

### Acoustic impedance matching

Owing to mismatched acoustic impedances, the ultrasound waves detected by PAI systems can generate strong reflection and distortion at the interfaces between soft tissue, bone, and gas. Thus, brain imaging researchers are working on correcting or mitigating such spurious photoacoustic signals arising from distortion by the skull<sup>232–235</sup>. For the same reason, all-optical ultrasound detectors are being developed for non-contact acoustic detection away from the tissue surface<sup>236,237</sup>.

### Quantification accuracy

The quantification accuracy of spectroscopic PAI requires improvement<sup>238</sup>. Accurate measurements of the absorption coefficients of specific chromophores is dependent on either knowledge or accurate estimation of the local optical fluence, which is proportional to the strength of the photoacoustic signal<sup>6</sup>. However, light propagating in the tissue is affected by spectrum-dependent attenuation, making the local optical fluence difficult to predict, especially in deep-tissue locations. To compensate for depth-related variations in optical fluence, one strategy determines light fluence in the spectral domain and introduces eigenspectra multispectral PAI to account for wavelength-dependent light attenuation<sup>239</sup>. Other solutions include measuring optical fluence using diffuse optical tomography<sup>240</sup> or estimation by Monte Carlo simulation<sup>241</sup>. Real-time PAI with simultaneous fluence compensation and motion correction has also been developed in an attempt to improve the reliability and accuracy of quantitative measurement<sup>242</sup>.

**Box 3 | Improvements in technology**

Photoacoustic imaging (PAI) technology combines optics, ultrasonography, mechanics, electronics and computer science. We anticipate that the performance of PAI can be further improved in the next decade by at least five developments:

**Stronger, faster and cheaper laser systems**

With a given laser pulse energy, a trade-off exists between imaging depth and the size of the field of view (FOV)<sup>22</sup>. Most pulsed lasers currently used in PAI systems are not specifically designed for this application. Thus the balance between performance and costs can be improved. For example, photoacoustic CT (PACT) usually does not require a laser system with a short pulse width (for example, <10 ns), narrow spectral linewidth or high coherence. Thus, with a laser that is optimized for pulse energy (such as 10 J) and repetition rate (such as 10 Hz), a PACT system will be able to provide a larger FOV (such as 12 cm in diameter) with similarly deep penetration and high acquisition speed.

**More sensitive acoustic detectors**

With sensitivity improvements in ultrasonic detectors, PAI could potentially recover weaker signals from deeper tissue locations. Although piezoelectric transducers (PZTs) are most commonly used for biomedical imaging, capacitive and piezoelectric micromachined ultrasonic transducers (CMUTs and PMUTs) have developed rapidly owing to their miniature size and high level of compatibility with integrated circuits. Specifically, PMUTs typically provide better sensitivity than conventional PZTs owing to their lower level of mechanical impedance<sup>243,244</sup>. Also, optical acoustic sensors (such as Fabry–Pérot interferometers) have been considered for decades owing to their broad bandwidths and high sensitivity at high frequencies<sup>111,245</sup>. However, such sensors are often affected by practical challenges such as scalability, availability and unclear reliability.

**Image reconstruction algorithms**

Currently, the universal back-projection reconstruction algorithm is widely used owing to ease of implementation and reliable performance. Nonetheless, more sophisticated algorithms using iterative reconstruction<sup>246</sup> or machine learning<sup>247,248</sup> are under development in an attempt to improve the image quality, especially to reduce the dependence on dense spatial sampling, the need for entirely motion-free study participants, and the preference for homogeneous acoustic properties.

**Regulations and standards**

Several research groups are developing PAI systems with vying levels of performance. Therefore, additional efforts are required to regulate this technology by standardizing and integrating the most advanced accomplishments in system design, operation and data processing. The International Photoacoustic Standardisation Consortium<sup>99,249</sup> has been established for this purpose.

**Microwave-induced thermoacoustic imaging**

Pulsed microwave illumination (within the established safety limits of radiation exposure)<sup>250</sup> can penetrate more deeply than near-infrared light and potentially enable whole-body imaging in patients with cancer. Unlike the optical absorption contrast provided by PAI, however, this imaging modality is reliant on dielectric contrast (from the ionic contents of water, lipids and other biomolecules) detected at microwave frequencies<sup>227,230</sup>.

flexibility, performance or simplicity. To further advance the utility of PACT for breast cancer screening, three types of guidelines are required: (1) engineering guidelines for reliable system performance (Supplementary Information); (2) operational guidelines for repeatability and safety; and (3) image reconstruction and data processing guidelines for measurement accuracy. These needs can be met by integrating the achievements of the most successful PAI systems and studies. An International Photoacoustic Standardization Consortium has been set up for this purpose<sup>99</sup>.

To complement current screening modalities, PAI approaches can be developed for imaging of tumour-associated angiogenesis and hypoxia, which can be combined with coregistered ultrasonography to improve early breast cancer detection in women with

radiographically dense breasts. For the same population in developing countries, breast screening is typically implemented using a hand-held ultrasonography scanning system, which is highly operator-dependent and is usually accomplished more rapidly than the standard protocol requirement (typically 13–15 min<sup>100,101</sup>). Accordingly, an opportunity exists for PAI to become established as the standard method of breast cancer screening in an enormous population.

**Skin cancer imaging**

Detection of skin cancer, including melanoma, is another area of active interest for researchers working on PAI systems<sup>102</sup>. Early lesion detection followed by surgical resection is the optimal method for reducing mortality from skin cancer. However, the selection of suspicious lesions for biopsy is somewhat subjective owing to a reliance on physician assessment, which also implies a risk of failing to detect cancerous lesions and unnecessarily excising benign moles<sup>103</sup>. Although high-frequency ultrasonography has been used for this purpose, this method usually lacks sufficient imaging contrast owing to limited variations in acoustic impedance<sup>104</sup>. PAI can provide additional contrast to complement ultrasonography-based measurements of the depth of measurable skin lesions. Preliminary studies demonstrate that PAI can distinguish between different kinds of skin tumours including primary or metastatic melanomas, basal cell carcinomas and squamous cell carcinomas by measuring the melanin, HbO<sub>2</sub>, HbR and collagen content of the lesions<sup>105,106</sup>.

Capitalizing on multiscale PAI, the feasibility of skin cancer imaging with both PAM and PACT has been demonstrated, and each of these modalities has distinctive advantages: PAM typically provides a high level of spatial resolution at lower cost<sup>107</sup>, while PACT usually enables a fast imaging speed and a larger FOV<sup>108</sup>. Here, we group PAI studies of the skin into those that focus on melanoma and those that focus on non-melanoma skin carcinoma (NMSC).

**Melanoma imaging.** Most melanomas contain melanin and manifest physiological changes; therefore, PAI of melanin and the surrounding vascular distributions (FIG. 3c,d) provides an unprecedented opportunity to understand the interactions between cancer and its microenvironment and for non-invasive cancer detection and staging<sup>27,109</sup>. By using a customized two-axis water-immersible scanning mirror for hand-held skin imaging, OR-PAM has been miniaturized, yielding a device with a 3D imaging rate of 2 Hz over a 2.5 × 2.0 × 0.5 mm<sup>3</sup> volume<sup>41</sup>. Further efforts reduced the size of the OR-PAM device to a probe with a diameter of 17 mm and a weight of 162 g, which is convenient for hand-held imaging of potentially suspicious lesions (such as moles) with a clear boundary and acceptable depth<sup>40</sup>.

As an alternative to PAM-based imaging, linear-array-based PACT was used to image pigmented cutaneous lesions, which are suspicious for melanoma, in 27 patients<sup>110</sup>. The thickness of lesions measured using PACT was strongly correlated with thickness measured after resection ( $r = 0.99$ ,  $P < 0.001$ , for melanomas;

$r=0.98$ ,  $P<0.001$ , for naevi). These results demonstrate the reliability of PACT in measuring cutaneous lesion thickness in patients. Furthermore, detailed imaging of lesional architecture can potentially be used to guide biopsy sampling procedures and improve cancer management.

**Non-melanoma skin cancer imaging.** In addition to imaging melanomas and lesions with a higher pigment concentration, spectroscopic PAI can also reveal the presence of NMSC from a haematogenous background. Investigators imaged the lesions of a total of 21 patients with NMSC, utilizing the high-resolution multispectral optoacoustic tomography (MSOT) system developed by Rasanzky and colleagues, which enables imaging at centimetre-scale depth<sup>26</sup>. Furthermore, this approach enabled the anatomy and oxygenation status of the tumours to be measured without the need for exogenous contrast agent (FIG. 3e). MSOT-based

measurements of tumour dimensions showed a good correlation with histology (intraclass correlation coefficient (depth and length) 0.81). Real-time 3D PAI showing the lesions' morphology and underlying neovascularity provided further indications of tumour aggressiveness.

Fabry–Pérot interferometers (FPI) have been applied for planar-view PACT to provide higher levels of detection sensitivity than that of traditional piezoelectric transducers<sup>111,112</sup>. The transparency of the FPI sensor enables the transmission of light, making this approach compatible with multiple optical clinical imaging modalities (such as optical coherence tomography). FPI-based PACT can enable 3D imaging of human skin and has been used to image a surgical scar and a basal cell carcinoma in a proof-of-principle study<sup>113</sup>. Vascular morphological and tortuosity parameters, such as vascular density, sum of angles and inflexion count, were measured to characterize the lesions.

To further advance the utility of PAI for skin cancer imaging, the characteristic measurements provided by this approach need to be correlated with physiological and pathological features. For example, PAI features, including tumour dimensions, tumour shape, blood vessel density, vessel distribution randomness, vessel morphological deformation, haemoglobin oxygen saturation, oxygen extraction fraction, total haemoglobin concentration and relative elasticity could be recorded in large-cohort prospective clinical trials. The value of, and changes in, each feature could then be evaluated and compared with the histopathological diagnosis. Related features could be further used to generate a multivariate model for screening and/or diagnosis.

#### Prostate cancer detection

Prostate cancer is the second most common cancer in men after NMSC. Early detection of the tumour, when it is still confined to the prostate gland, provides the best opportunity for successful intervention. Currently, prostate cancer is usually detected following elevation of serum prostate-specific antigen levels on routine testing, or presentation with related urological symptoms<sup>114</sup>. Digital rectal examination, often followed by MRI or PET can provide a high detection rate and enable accurate assessments of prostate cancer aggressiveness, although these methods are not suitable for regular screening, monitoring or real-time biopsy guidance.

Transrectal ultrasonography (TRUS) is used clinically to complement MRI and PET. Although TRUS alone is not sufficiently reliable for prostate cancer imaging, it is an ideal platform for integrating functional and molecular imaging modalities for improved cancer detection. An endoscopic probe that combines TRUS with PAE has been developed and tested for this purpose in a proof-of-principle study<sup>4</sup>. Sharing a micromachined ultrasonic array with the TRUS setup, the miniaturized PAE endoscope enabled simultaneous imaging of the haematogenous and molecular optical contrasts of the human prostate (FIG. 3f). Haemoglobin absorption was used to map the vasculature, and ICG absorption was used to enhance the intraprostatic photoacoustic contrast from vasculature structures. The additional

#### Box 4 | Current and future clinical applications

By improving the technical performance, information richness and operational reliability, more clinical investigators will probably use, report and thus extend the spread of this technology from the application perspective. Spurred by advances in photoacoustic imaging (PAI), clinics are likely to pay more attention to haemoglobin-related physiological imaging features and how these relate to cancer progression. In addition to such endogenous contrasts, FDA-approved contrast agents that absorb light at certain wavelengths can be imaged using targeted PAI approaches. We anticipate that the following applications of PAI will provide clinical oncologists with more useful information and distinctive advantages:

##### Breast cancer

PAI can contribute to early detection, accurate diagnosis and precise treatment assessments. Equipped with high-speed scanning and using only non-ionizing radiation, PAI can potentially detect cancers with a high level of sensitivity, even in women with dense breasts, and improve the specificity of standalone ultrasonography. In performance terms, PAI provides a faster, clearer but also more portable version of contrast-enhanced MRI and can be used both to diagnose lesions and to evaluate responses to treatment by adding haematogenous information to ultrasound images.

##### Skin cancer

PAI can penetrate more deeply than other optical microscopic modalities while providing more detailed physiological information than ultrasonography. Such unique functional optical contrast, depth and clarity can potentially improve the selection of suspicious lesions for biopsy sampling. Combining PAI with photothermal and photodynamic therapies could further enable PAI to reveal both pharmacokinetic and pharmacodynamic processes as well as to provide information on prognosis.

##### Cancers of internal organs

Photoacoustic endoscopy (PAE) can potentially enable screening for cancers of the rectum, oesophagus, prostate and thyroid. PAE might provide better specificity than endoscopic ultrasonography owing to its ability to reveal additional physiological information.

##### Intraoperative cancer management

PAI can provide fast cancer margin examination without the need for fixing or staining. Furthermore, targeted imaging using contrast agents will clearly delineate the mass in three dimensions for precise surgical guidance in scenarios where resection is particularly challenging (such as neurosurgery). Real-time tracking of surgical tools, biopsy needles and their positions relative to the targets is likely to improve the efficacy of the procedure.

##### Paediatric cancers

PAI for cancers in children and young adults is an area worthy of greater investigation, PAI is appealing owing to the ability to achieve high levels of spatiotemporal resolution without the need for ionizing radiation, sedation or contrast agent injection.

ability to image ICG uptake would further help to elucidate the malignant region.

By providing real-time anatomical, functional and molecular imaging of the human prostate, PAE has the potential to be adopted into routine clinical workflows. From the engineering perspective, the imaging performance of PAE could be improved by optimizing the optical illumination and acoustic detection schemes<sup>115</sup>. Most PACT-based PAE systems currently use ultrasonic arrays and data acquisition circuits that are not optimized for PAI, thus resulting in compromised image quality owing to the limited view angle and high level

of noise<sup>35,116–118</sup>. Nonetheless, the experience with imaging of other internal organs suggests that minor modifications of the PAE probe might ameliorate these issues (as seen with PAE systems designed for the rectum<sup>119</sup> and oesophagus<sup>120</sup>).

**PAI of other cancers**

PAI was originally conceived to bridge the gap in scale between optical microscopy and whole-body imaging scans, while also providing physiological information based upon differences in contrast. Accordingly, PAI has the potential to reveal many other types of cancer growing

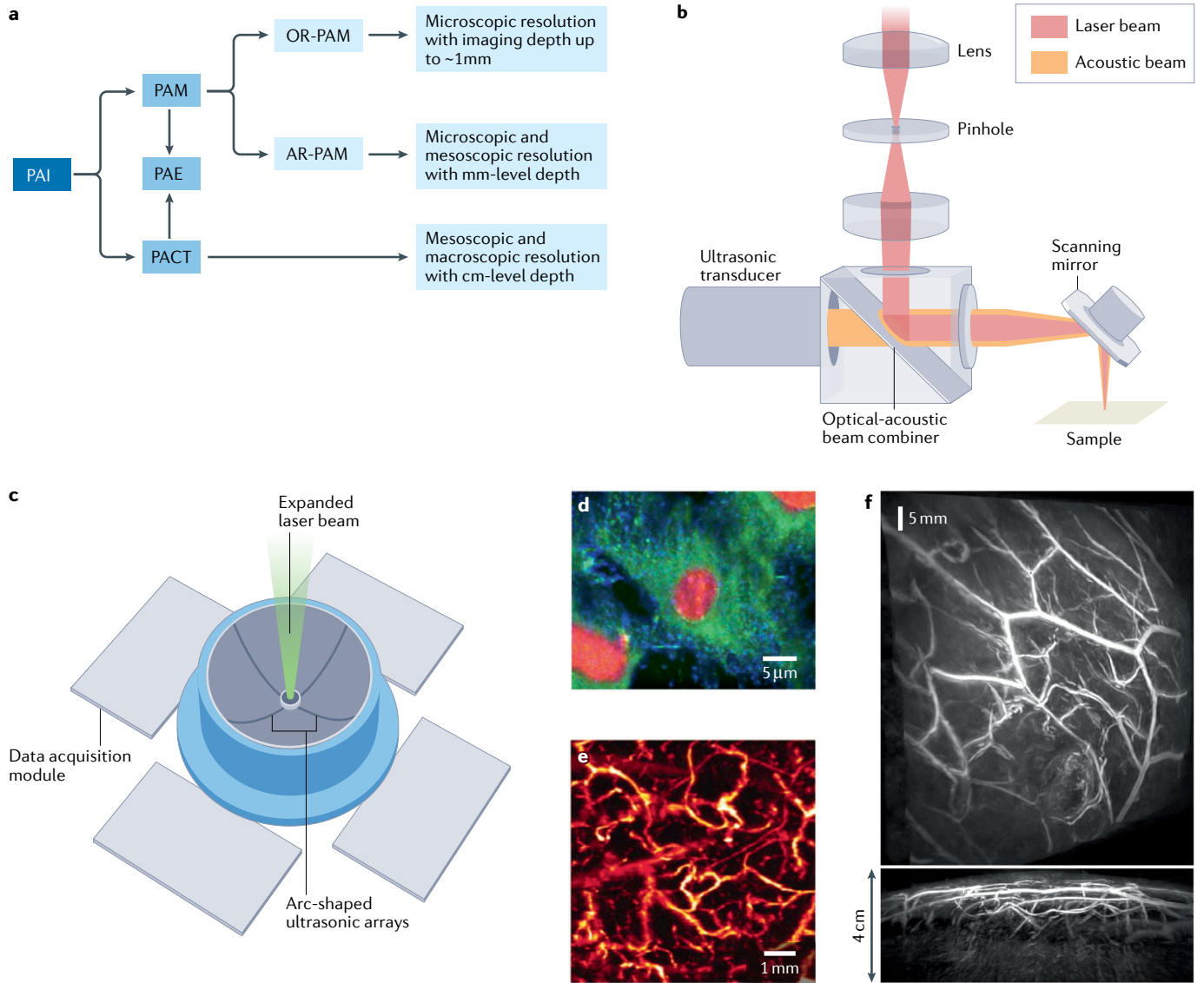


**Fig. 1 | Representative configurations and images of photoacoustic imaging.** **a** | Overview of the main photoacoustic imaging (PAI) configurations and imaging scales. Photoacoustic endoscopy (PAE) is essentially a miniaturization of photoacoustic microscopy (PAM) or photoacoustic CT (PACT). **b** | Schematic of a typical reflection-mode optical resolution (OR)-PAM system, featuring an optical-acoustic beam combiner that reflects light but transmits sound<sup>39</sup>. **c** | Schematic of a 3D PACT system with four arc-shaped ultrasonic arrays<sup>39</sup>. A coaxial rotation of the four arrays forms a densely sampled hemispherical detection matrix. The laser beam is expanded to provide wide-field illumination<sup>1</sup>. **d** | Mid-infrared OR-PAM

image of lipids (blue), proteins (green) and nucleic acids (red)<sup>49</sup>. **e** | Acoustic resolution (AR)-PAM image of a human palm showing the distribution of blood vessels located under the skin surface<sup>2</sup>. **f** | PACT angiogram of the right breast of a woman without cancer; the bottom image depicts a maximum-amplitude projection of the same breast, viewed from the side. An imaging depth of 4 cm below the skin surface has been achieved<sup>1</sup>. Part **b** is adapted from REF.<sup>39</sup>, Wiley; part **c** is adapted from REF.<sup>1</sup>, CC BY 4.0; part **d** is adapted from REF.<sup>49</sup>, Springer Nature; part **e** is adapted from REF.<sup>2</sup>, CC BY 4.0; and part **f** is adapted from REF.<sup>1</sup>, CC BY 4.0 (<https://creativecommons.org/licenses/by/4.0/>).

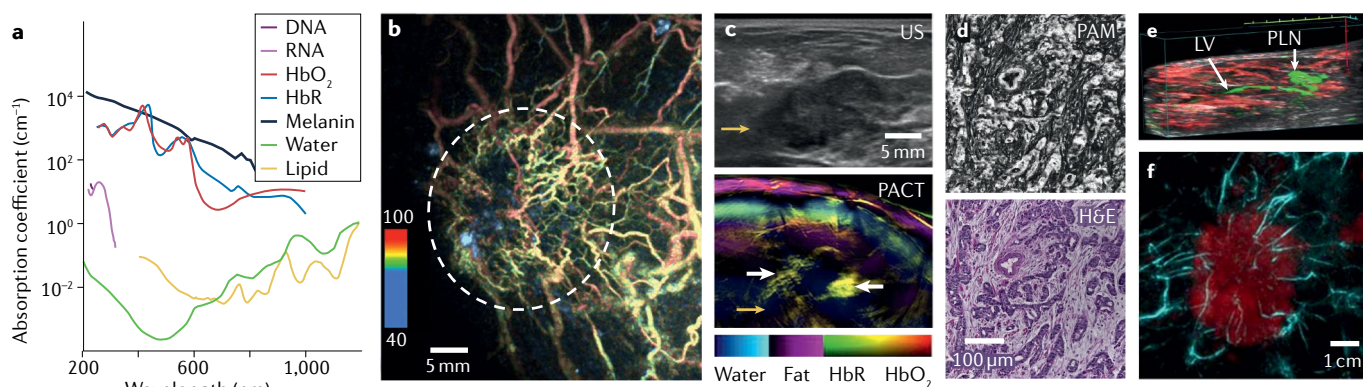


**Fig. 2 | Representative photoacoustic contrasts in biological tissues.**

**a** | Absorption coefficient spectra of endogenous tissue chromophores, including DNA, RNA, oxyhaemoglobin (HbO<sub>2</sub>), deoxyhaemoglobin (HbR), melanin, water and lipids<sup>224</sup>. **b** | Photoacoustic CT (PACT) clearly reveals the angiogenesis associated with a tumour in a patient with breast cancer. The use of pseudocolours reflects the relative oxygen saturation. Here, red indicates arteries, and yellow and green indicate veins<sup>97</sup>. **c** | Ultrasound (US) image of an invasive lobular breast carcinoma in a patient with breast cancer, indicated by the yellow arrow. The bottom image depicts a multicontrast photoacoustic image of the same tumour (white arrow) showing strong photoacoustic signals at the image boundaries (white arrows)<sup>91</sup>. **d** | Optical resolution photoacoustic microscopy (PAM) of breast tissue slices acquired without staining (top), showing a high correlation with haematoxylin and eosin

(H&E)-stained histological images (bottom)<sup>30</sup>. **e** | PACT image depicting indocyanine green (ICG, green) and blood vessels (red)<sup>61</sup>. The grey colour map represents the ultrasound signal. ICG indicates the presence of lymphatic vessels (LV) and a popliteal lymph node (PLN). **f** | Fusion of images acquired using PACT (cyan) and MRI (red). Tumour-related blood vessels converge from the non-malignant breast tissue towards the centre of the tumour, becoming narrower at the tumour edge and almost vanishing near the centre<sup>62</sup>. Part **a** is adapted from REF.<sup>224</sup>, CC BY 4.0; part **b** is adapted from REF.<sup>97</sup>, CC BY 4.0; part **c** is adapted from REF.<sup>91</sup>, CC BY 4.0; part **d** is reprinted from REF.<sup>30</sup> (copyright the authors, some rights reserved; exclusive licensee the American Association for the Advancement of Science), distributed under a CC BY-NC 4.0 license; part **e** is reprinted from REF.<sup>61</sup>, CC BY 3.0; and part **f** is reprinted from REF.<sup>62</sup>, CC BY 4.0 (<https://creativecommons.org/licenses/by/4.0/>).

within reach of light (within the optical dissipation limit<sup>10</sup>) from either external or internal surfaces. To date, PAI has been used to image thyroid<sup>121</sup>, ovarian<sup>122,123</sup> and cervical cancers<sup>124</sup> *ex vivo*, and is moving towards clinical practice. For example, spectroscopic PAI has been used to quantify the deoxyhaemoglobin content of 13 malignant and 75 benign thyroid lesions immediately after thyroidectomy<sup>125</sup>, indicating potential utility in the assessment of suspicious lesions. For cancers growing in the rectum and oesophagus, where lesions are easily overlooked until abnormal symptoms appear, PAI could be developed as a standardized screening modality by improving upon the sensitivity and specificity of endoscopic ultrasonography, similar to the role of PAI in breast cancer screening. In addition to direct imaging of solid tumours, a photoacoustic spectrometer has been developed as a method of early lung cancer detection, based on measuring levels of acetone in exhaled air<sup>126</sup>. To foresee suitable applications of PAI in clinical oncology, one should first determine the useful information or distinctive improvements that PAI approaches might provide and are currently unavailable or impractical with other technologies.

### Cancer diagnosis

Both screening and diagnosis are essential for comprehensive cancer control: diagnostic investigations typically involve patients with suspicious screening findings or who have symptoms that might be suggestive of cancer. Accordingly, diagnostic tests are generally more invasive and time-consuming. For discussion, here we group major PAI studies on cancer diagnosis into four categories: breast cancer diagnosis, melanoma metastases detection, biopsy guidance and the emerging role of molecular PAI enabled by various contrast agents.

### Breast cancer diagnosis

The angiographic and functional information provided by PACT directly relates to breast tumour pathophysiology, and supports clinical decision-making regarding the malignant potential of a specific lesion and the need for biopsy sampling<sup>127,128</sup>. This principle has been demonstrated by the commercial availability of a hand-held PACT-ultrasonography device manufactured by Seno Medical Instruments<sup>129–132</sup> (FIG. 4a,b). Using this probe, investigators in the PIONEER study imaged 1,690 women with a total of 1,757 breast masses initially identified using ultrasonography and classed as Breast Imaging Reporting and Data System (BI-RADS) 3, 4 or 5 including 1,079 benign lesions and 678 malignant lesions. The addition of PACT improved the diagnostic specificity of stand-alone ultrasonography by 14.9% ( $P < 0.0001$ )<sup>130</sup>. The same imaging system was further applied to image 209 patients with 215 breast masses classified as BI-RADS 4a or 4b by ultrasonography<sup>131</sup>. Researchers scored each lesion based on five PACT features, including: (1) internal vascularity and deoxygenation, (2) internal blush (probably owing to the resolution limitation) and deoxygenation, (3) internal HbT, (4) boundary zone vasculature, and (5) peripheral zone radiating vasculature. Using a weighted sum of the five feature scores, researchers estimated the probability of malignancy on a scale from 0% to 100% and adjusted the previous conventional ultrasonography-assigned BI-RADS classification. In this landmark study, which was designed to simulate a real-world clinical workflow, 41% of benign masses were correctly downgraded from BI-RADS 4a or 4b to BI-RADS 3 or 2 by PACT-ultrasonography, highlighting a potential decrease in the number of biopsy samples with negative findings and the need for follow-up imaging

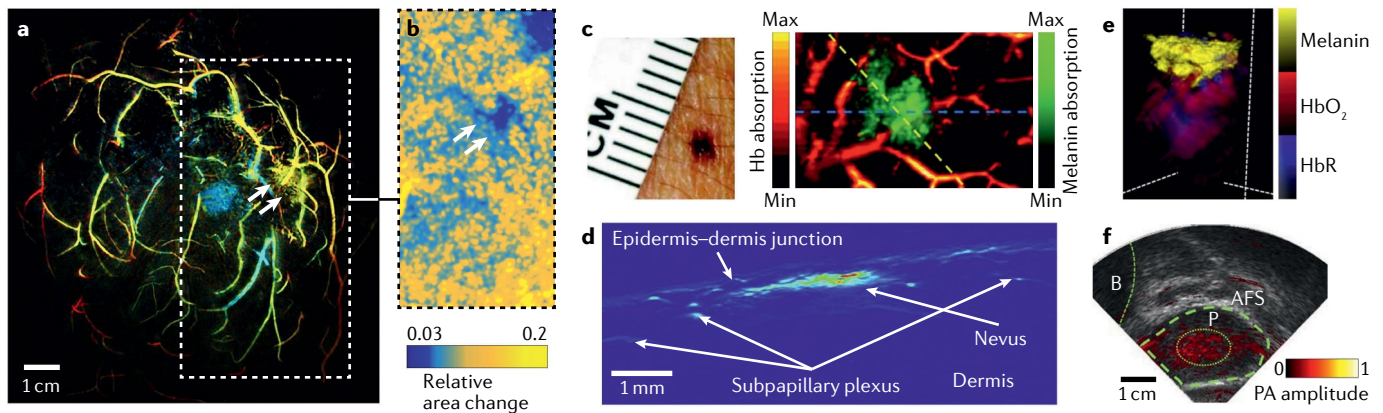


**Fig. 3 | Representative in vivo photoacoustic imaging for cancer detection.** **a** | Depth-encoded angiograms of a malignant breast acquired using photoacoustic CT<sup>5</sup>. The breast tumour (invasive ductal carcinoma, grade 2) is indicated by the white arrows. **b** | Photoacoustic elastography in the region outlined by the dashed box in part **a**, showing the relative area change during breathing<sup>5</sup>. The same tumour is indicated using white arrows. **c** | Left, photograph of a naevus located on the forearm of a human patient. Right, acoustic resolution photoacoustic microscopy image (right) with dual contrasts of the melanin (green) and haemoglobin distributions (red) near the naevus<sup>3</sup>. Melanin is the primary optical absorber in melanoma. **d** | Cross-sectional photoacoustic image taken along the blue dashed line in part **c**, showing the melanin

distribution in the depth direction<sup>2</sup>. **e** | Volumetric image of a basal cell carcinoma (non-melanoma skin cancer) acquired in vivo from a human patient<sup>26</sup>. Melanin signals are clustered at the top, with strong haemoglobin signals underneath the lesion. **f** | Transrectal photoacoustic and ultrasonography images of the prostate in a patient with prostate cancer<sup>4</sup>. AFS, anterior fibromuscular stroma; B, bladder; Hb, haemoglobin; HbO<sub>2</sub>, oxyhaemoglobin; HbR, deoxyhaemoglobin; P, prostate (green dashed contour). Parts **a** and **b** are reprinted from REF.<sup>5</sup>, CC BY 4.0; parts **c** and **d** are adapted from REF.<sup>2</sup>, CC BY 4.0; part **e** is reprinted from REF.<sup>26</sup>, CC BY 4.0 (<https://creativecommons.org/licenses/by/4.0/>); and part **f** is adapted with permission from REF.<sup>4</sup>, American Association for the Advancement of Science.

examinations. After readjusting the image interpretation standard, a 98.5% true-positive rate was achieved. These data are supported by the findings of the READER-02 study<sup>133</sup>, which involved the analysis of a subset of images from the PIONEER study and demonstrated that the addition of PACT to standard ultrasonography confers a statistically significant improvement in the specificity of diagnosis, from 38.2% to 47.2% ( $P=0.027$ ) at a fixed sensitivity of 98%.

Owing to the limited-view acoustic detection<sup>134,135</sup>, the linear-array-based PACT approach used in these studies could not reveal features with isotropic clarity. Therefore, enlargement of the acoustic detection view angle of the PACT-ultrasonography probe could further reduce the risk of false-negative findings (or improve the specificity) by providing better image clarity. Nonetheless, this breast imaging system was approved in January 2021 by the FDA for the assessment of BI-RADS 3–5 masses following initial ultrasonography, and is the first FDA-approved PAI system for any medical indication<sup>31,133</sup>. Once large amounts of open-source data become available, machine learning can be introduced to assess PACT image features and might enable further improvements in tumour segmentation and image interpretation.

Clinical studies performed by other groups have confirmed the diagnostic value of PACT-based imaging in breast cancer by demonstrating statistically significantly lower sO<sub>2</sub> levels and distributions in malignant than in benign masses ( $P<0.001$  for both comparisons)<sup>136–138</sup>. In addition to the interior regions of the tumour, data from multiple studies involving spectroscopic PACT also show differences in the distributions of photoacoustic signals from the boundary regions of benign and malignant breast lesions<sup>131,136,139</sup>. Specifically, the volumetric mean sO<sub>2</sub> in stage T1 invasive breast carcinoma

was found to be 7.7% lower than in benign tumours ( $P=0.016$ ) and 3.9% lower than in non-malignant breast tissues ( $P=0.010$ )<sup>139</sup>. The volumetric mean sO<sub>2</sub> in tumours surrounding regions of stage T1 invasive carcinoma was 4.9% lower than in benign tumours ( $P=0.009$ ). In particular, the peripheral zone of malignant tumours tended to have a more diffuse vasculature (blood vessels radiating both towards and away from the tumours)<sup>131</sup> and a lower mean sO<sub>2</sub> (FIG. 4c). These distinctive imaging features derived from PACT provide additional criteria for a more accurate diagnosis. Owing to the strong correlations between breast tumour angiogenesis and metastasis<sup>47,90</sup>, PACT can potentially enable the risk of metastasis to be evaluated and thus reduce the number of patients receiving a false-negative diagnosis<sup>129</sup>. In addition to a single test, PACT can also be safely used for high-speed serial imaging, to monitor indeterminate breast lesions<sup>140</sup>.

For wider clinical adoption, how photoacoustic measurements correlate with clinical characteristics will need to be investigated further to enable standardized interpretation. Engineers developing PAI systems also need to understand the relevant clinical workflows in order to fulfil the potential of PAI to enhance current diagnostic strategies and improve both patient management and treatment outcomes. At present, most large-scale clinical trials of breast PAI involve imaging systems that could be further optimized for better clarity, deeper tissue penetration, a larger FOV and higher speed.

#### Detection of melanoma metastases

The presence of lymph node metastases is one of the essential criteria in melanoma staging<sup>141</sup>. Although effective, lymph node excision is an invasive procedure requiring injection of a radioactive tracer. In comparison, a non-invasive imaging modality that enables

the accurate detection of metastases could reduce the need for invasive excision surgery for biopsy sampling of potentially benign lymph nodes. In a clinical study involving 214 patients with melanoma, multispectral PACT improved the tumour metastasis detection rate in examinations of excised sentinel lymph nodes (SLNs) compared with the conventional imaging protocol (22.9% versus 14.2%)<sup>28</sup>. Furthermore, when ICG was used to enhance the imaging contrast of SLNs, researchers were able to image SLNs in 20 patients (FIG. 4d) with 100% concordance with <sup>99m</sup>Tc-marked SLN lymphoscintigraphy. The authors also claimed to have identified cancer-free SLNs both in patients and in excised material with 100% sensitivity and 48–62% specificity.

Along with imaging lymph node metastases, the improved imaging contrast provided by PAI enables circulating melanoma cells (CMCs) present in the bloodstream to be visualized and tracked. For this purpose, investigators developed a flow cytography approach based on high-speed OR-PAM coupled with melanoma-specific localized laser therapy<sup>142</sup>. Following in vivo label-free imaging of CMCs in mice, a lethal pin-point laser irradiation was immediately triggered by the photoacoustic signal from the melanoma cell, which was thermally killed without collateral damage. The same research group also imaged CMC clusters in patients using linear-array-based PACT<sup>29</sup> (FIG. 4e). Among the 16 patients with stage III or IV melanoma, CMCs were detected in three patients, two of whom had disease progression (diagnosed shortly before undergoing PAI). At the same time, nine of 13 CMC-negative patients did not have disease progression. With the addition of a stronger laser and more sensitive acoustic detection, PACT could be used to detect melanoma metastasis more accurately and thus improve patient prognosis.

### Guidance for biopsy

In addition to direct detection of metastases, PAI-guided biopsy sampling could be merged into the current clinical workflow. The available non-invasive imaging modalities (ultrasonography, CE MRI, contrast-enhanced CT and PET) generally lack sufficient accuracy<sup>143</sup>, therefore, lymphadenectomy remains the gold standard method of lymph node assessment and staging. Compared with lymphadenectomy, SLN biopsy sampling is a less invasive method of predicting the pathological status of the axilla. However, owing to a lack of imaging contrast, SLNs are currently identified intraoperatively, thus increasing the risk of morbidities<sup>144</sup>. To address these limitations, investigators developed a dual-modality PACT–ultrasonography imaging system designed to non-invasively detect SLNs in patients with breast cancer based on accumulation of the FDA-approved dye methylene blue (FIG. 4f). This method showed higher levels of contrast in both the target SLN and the biopsy needle<sup>60</sup>. A similar imaging strategy has also been successfully demonstrated in animals using clinically approved carbon nanoparticles<sup>145</sup> and fluorescence dyes<sup>146,147</sup>. Technical improvements have since been made by introducing fast scanning of a linear array for needle tracking in the 3D space<sup>148</sup>. Researchers have also modified the biopsy needle by inserting an optical fibre

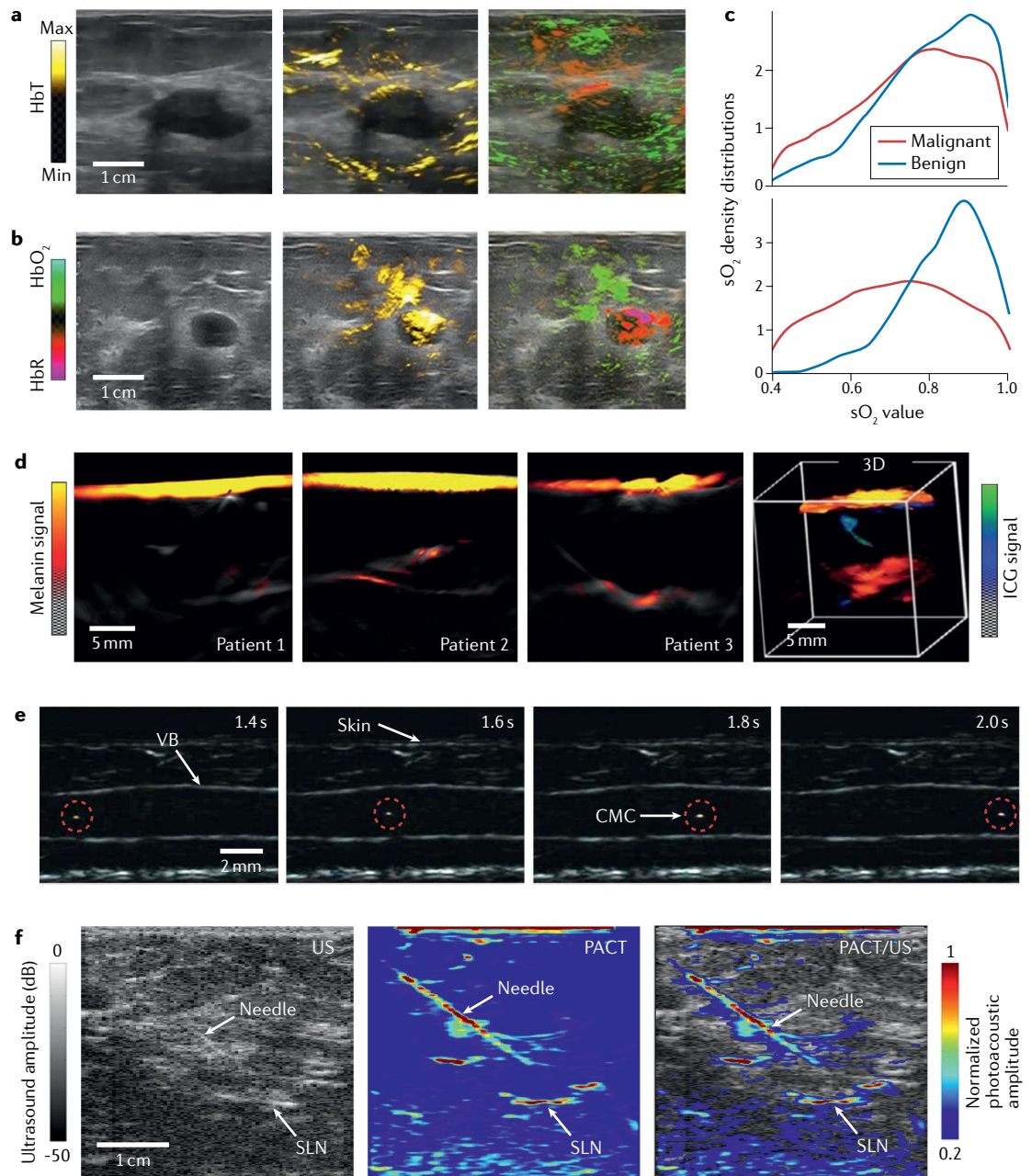
to provide deeper optical delivery<sup>149</sup>. Since the system relies on PACT for signal collection and image formation, inhomogeneous optical fluence near the fibre tip compromises the image quality<sup>22</sup>. Accordingly, this issue remains a barrier to the direct clinical implementation of PACT systems that involve the delivery of light through needles. To improve image clarity and performance reliability, dedicated PACT systems with optimized acoustic detection (for example, with an increased coverage angle<sup>34</sup>) and optical delivery (which could be achieved using a compressible fibre probe) need to be designed. The upgraded PACT system could be routinely used to guide minimally invasive SLN biopsy or fine-needle aspiration biopsy sampling.

### PAI of exogenous contrast agents

Unlike routine screening, diagnostic investigations are more likely to detect active malignancies. Therefore, the use of imaging modalities involving contrast agents is more acceptable for this purpose. Exogenous contrast agents have the potential to enable improved diagnostic accuracy, potentially leading to improved therapeutic efficacy<sup>150</sup>. Owing to this potential for greater molecular specificity, the use of PAI in conjunction with exogenous contrast agents is currently an area of considerable research interest<sup>13,51</sup>.

Several biocompatible small molecules (less than tens of nanometres in diameter) dyes<sup>151</sup>, such as ICG<sup>4</sup>, methylene blue<sup>60</sup> and IRDye800CW<sup>152</sup>, have been used safely in molecular PAI studies involving humans, and some success has been reached at the proof-of-concept stage<sup>8</sup>. In the past years, ICG has been modified to improve its biochemical properties and molecular imaging capability for diagnostic and therapeutic purposes. For example, the FDA-approved anti-EGFR antibody panitumumab labelled with an ICG derivative (ICG–EG4) has been used as a PAI probe to detect squamous cell carcinoma lesions in a mouse xenograft model<sup>153</sup>. These investigators used an in vivo PAI approach and inhibition studies with unlabelled panitumumab to demonstrate that ICG-labelled panitumumab specifically targets EGFR-expressing A431 cells. Notably, panitumumab is currently only approved for patients with colorectal cancer<sup>154</sup>, which would necessitate PAE-based imaging via colonoscopy<sup>119</sup> to identify EGFR-expressing tumours and thus guide the selection of targeted therapies. More recently, PAI of ICG conjugated to a specific antibody against the B7-H3 receptor, a potential target identified in patients with breast cancer (expressed on 57% of breast cancer cells versus 43% of adjacent non-malignant cells;  $P < 0.05$  (REF. 155)), has been used to distinguish human breast tumour tissue from non-malignant breast tissue samples<sup>156</sup>. In a relevant transgenic mouse model of breast carcinoma, antibody–ICG conjugates were found to undergo spectral shifts in optical absorption, with specific accumulation in breast cancer lesions. Accordingly, PAI using this targetable ICG conjugate could improve the detection and diagnosis of breast cancer.

PAI with exogenous contrast agents is still in the early stages of clinical development, although PAI studies involving various FDA-approved contrast agents have



demonstrated the diagnostic potential of this approach. For example, PAI of ICG uptake and extravasation in breast cancer, in principle, provides a cheaper, faster and higher-resolution alternative to gadolinium-based CE MRI<sup>59</sup>. While the current clinically available contrast agents were not specifically designed for use in conjunction with PAI systems, molecular PAI still has a potential role in precision medicine, especially with the approval of a greater number of contrast agents, which measure an ever-wider range of biomarkers.

**Cancer treatment assessment and guidance**

In addition to cancer screening and diagnosis, PAI also has a potential role in guiding and assessing the effects of cancer treatment. Here, we discuss this potential in three areas: assessing the effects of neoadjuvant chemotherapy; guiding surgical resection; and monitoring drug

delivery. Descriptions of the latter two of these areas are further subdivided based on the choice of imaging contrast agent.

**Response to neoadjuvant chemotherapy**

The survival outcomes in patients with breast cancer have been improved by the development and increased use of systemic therapy. These improvements include the development of neoadjuvant chemotherapy, a systemic treatment given before surgery, which can increase the likelihood of breast conservation and might also enable downstaging, whereby patients with disease deemed unresectable can become eligible for surgery<sup>157</sup>. Identifying patients with an early response to neoadjuvant chemotherapy provides important prognostic information and enables clinicians to optimize and personalize the treatment approach<sup>158</sup>. Similarly, rapid

◀ **Fig. 4 | PAI for cancer diagnosis.** **a** | A benign fibroadenoma, downgraded following photoacoustic CT (PACT)<sup>129</sup>. The ultrasonography (US) image (left) shows an indeterminate lobulated hypoechoic solid breast mass that was classified as 4a using the Breast Imaging Recording and Data System (BI-RADS). PACT–ultrasonography combined maps show a lack of microvasculature within the tumour (middle) and a normally oxygenated mass (right). These PACT features suggest the presence of a benign mass, such as a fibroadenoma. This mass was correctly downgraded from BI-RADS 4a (with ultrasonography only) to BI-RADS 3 using PACT–ultrasonography (biopsy-confirmed). **b** | A grade 3 invasive ductal carcinoma that was upgraded from BI-RADS 3 on ultrasonography to BI-RADS 5 on PACT–ultrasonography<sup>129</sup>. Conventional ultrasound morphology (left) shows an oval well-circumscribed hypoechoic mass located in the right breast. These imaging features suggest the presence of a benign lesion, such as a fibroadenoma. PACT–ultrasonography, however, reveals a substantial increase in haemoglobin content (middle) and a hypoxic vasculature indicated in red (right). PACT features suggest the presence of an active carcinoma, which was confirmed by analysis of a biopsy sample obtained after diagnostic imaging. **c** | The sO<sub>2</sub> density distribution in the tumour regions (top) and tumour-surrounding regions (bottom) of an invasive breast cancer (red lines) and a breast fibroadenoma (blue lines)<sup>139</sup>. **d** | PACT images of the sentinel lymph nodes (SLNs) in a patient with no detectable metastasis (patient 1), a patient with pigmented cells in the SLN, where no evidence of metastasis was found on histology (patient 2), and a patient with a positive SLN confirmed by immunohistochemistry (patient 3)<sup>28</sup>. The volumetric image on the right shows both melanin and indocyanine green (ICG) distributions in the SLN. **e** | In vivo PACT snapshots of a melanoma circulating cell cluster in the bloodstream of a patient<sup>29</sup>. The right image is a coregistered PACT–ultrasonography image of the SLN and needle. The red dashed circles highlight the melanoma cell cluster. **f** | In vivo images of an SLN and biopsy needle, acquired using ultrasonography (left) and PACT (middle) in real-time<sup>60</sup>. CMC, circulating melanoma cell; HbO<sub>2</sub>, oxyhaemoglobin; HbR, deoxyhaemoglobin; HbT, total haemoglobin; VB, vessel boundaries. Parts **a** and **b** are reprinted from REF.<sup>129</sup>; part **c** is reprinted from REF.<sup>139</sup>; part **d** is adapted with permission from REF.<sup>28</sup>, American Association for the Advancement of Science; part **e** is reprinted from REF.<sup>29</sup>; and part **f** is adapted from REF.<sup>60</sup>, CC BY 4.0 (<https://creativecommons.org/licenses/by/4.0/>).

evaluation of the effectiveness of novel therapeutic agents in this setting requires accurate imaging strategies to monitor the tumour response<sup>159</sup>. Non-invasive clinical imaging methods are currently dependent on tumour morphology and size measurements, which might not comprehensively reflect a response to therapy. Furthermore, therapy-induced fibrosis often impedes the ability to obtain accurate measurements using standard clinical imaging approaches<sup>160</sup>.

Comparable to a contrast-free, high-speed and high-resolution version of MRI, a breast PACT imaging system has been used for tumour imaging in three patients with breast cancer at three different time points: before, during and after neoadjuvant chemotherapy<sup>161</sup> (FIG. 5a). Analyses of tumour diameter, vascular density, and vascular distribution and morphology provided accurate indications of the response to neoadjuvant chemotherapy, as confirmed by histopathological analysis. In addition to monitoring detailed angiographic alterations, a decrease in intratumoural HbT and sO<sub>2</sub> was observed in a patient with breast cancer imaged using PACT<sup>162</sup>. To implement these observations, a larger-scale clinical study is needed, using a high-performance PACT system that can reveal both the detailed anatomy and subtle functional changes associated with breast cancer. Owing to the small diameters of many of the lesions, the high level of detection sensitivity provided by PACT could be used to non-invasively confirm the complete eradication of all tumour material (to determine a pathological complete response). A diagnostic scheme based on PACT features would also need to be established

and integrated into the current clinical workflow for neoadjuvant therapy.

### Guidance for surgical resection

The roles of PAI in surgery can be separated into ex vivo examination of the tumour margins in surgical specimens and in vivo guidance in localizing the lesion. For in vivo guidance, PAI can image either endogenous or exogenous contrast, revealing anatomical, functional and molecular information that can enable more accurate and safer excision<sup>163</sup>.

**Intraoperative cancer margin examination.** Instead of removing the entire breast tissue during mastectomy, 60–75% of patients with breast cancer will undergo breast-conserving surgery with the aim of removing the tumour and surrounding tissue only. Current clinical practice is to rely on histological analysis of the surgical specimen after completion of surgery to confirm that complete excision of all cancer cells has been achieved<sup>164</sup>. This approach implies that patients with cancer cells detected at the specimen margins will require additional surgery. At present, no intraoperative tools capable of microscopically analysing an entire lumpectomy specimen are available, resulting in 20–60% of patients undergoing second surgical procedures<sup>30</sup>. By taking advantage of the intrinsic optical contrast of biological tissues, UV light can highlight the presence of cell nuclei<sup>165</sup>, thus providing the same level of contrast as the haematoxylin labelling used in conventional histology while requiring no staining or labelling<sup>30</sup> (FIG. 2d). Therefore, UV light-excited OR-PAM could be used intraoperatively to guide immediate re-excision and thus reduce the number of second procedures. The same group that initially reported this possibility has since improved the speed of this imaging approach by applying microlens and linear ultrasonic arrays for parallel excitation and detection<sup>166</sup>. This system is capable of scanning a mouse brain slice with an image acquisition time of 16 min, suggesting early promise for the intraoperative assessment of surgical margins. Faster scanning approaches<sup>38</sup> and computer-aided diagnosis are being developed to better fulfil clinical needs, and imaging specificity can be further improved by using multiwavelength illumination. For example, by adding 700-nm light excitation, microcalcifications can be revealed with increased imaging depth<sup>167</sup>. Intraoperative OR-PAM can be used to acquire images of tumour histology without the need for fixation or further processing of the surgical specimen, although this method usually introduces blank regions into the image. Deep learning methods might be helpful in analysing these images, particularly for pathologists who are used to analysing sliced specimens.

**Label-free PAI for real-time guidance.** With the development of minimally invasive surgical procedures, an increasing need for precise imaging-based guidance exists. PAI, coupled with ultrasonography, naturally provides dual-modality imaging with the addition of functional optical contrast. For example, the real-time monitoring of sO<sub>2</sub> distribution in surgical regions would facilitate tumour resection with minimal invasion of

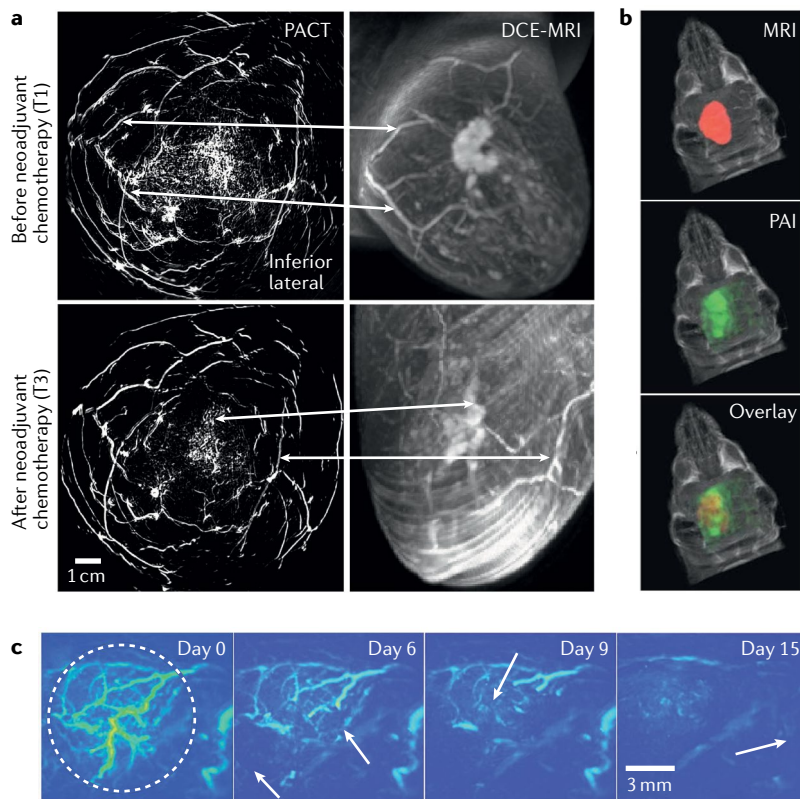


**Fig. 5 | Photoacoustic imaging for assessment and guidance of cancer treatment.** **a** | Human breast images acquired using photoacoustic CT (PACT) and dynamic contrast-enhanced MRI (DCE MRI) before and after neoadjuvant chemotherapy<sup>161</sup>. Correlated structures are marked by white arrows. PACT reveals a greater level of angiographic details within a single breath-hold of 15 s. **b** | MRI (top) and photoacoustic image (PAI, middle) of a mouse model of glioblastoma labelled with silica-coated gold nanoparticles<sup>177</sup>. An overlaid image (bottom) of the photoacoustic signal (green) laid over the MRI (red) shows good colocalization of the two imaging modalities. **c** | PACT monitoring of the therapy response of a tumour on different days following injection of plasmonic gold nanostars<sup>183</sup>. Arrows indicate the presence of vascular alterations during photothermal therapy. Part **a** is reprinted from REF.<sup>161</sup>, CC BY 4.0 (<https://creativecommons.org/licenses/by/4.0/>); part **b** is adapted from REF.<sup>177</sup>, Springer Nature; part **c** is reprinted with permission from REF.<sup>183</sup>, Wiley.

the adjacent non-malignant tissue<sup>168</sup>. Several research groups are currently exploring the role of PAI coupled with certain surgical tools, such as the robot-assisted surgery systems used for robot-assisted hysterectomy<sup>169,170</sup>. Although the reported rate of intraoperative ureteral injury is <0.78%<sup>171</sup>, 50–70% of such injuries are undetected during surgery<sup>172</sup>. The uterine arteries are usually cauterized during hysterectomy and PAI-based guidance of the procedure could potentially reduce the risk of accidental injury to the ureters<sup>173</sup>, which are located within millimetres of the arteries. Another example is the potential to reduce the risk of arterial injury in patients requiring surgical resection of pituitary tumours. Optical fibres can be coupled to a surgical tool introduced into the nose to illuminate the internal carotid arteries, which are detected using an external transcranial ultrasound probe placed at the patient's temple<sup>174,175</sup>. Nonetheless, more sophisticated PAI probes with higher levels of sensitivity and image quality are required to achieve further progress. For example, based on an FPI film sensor, investigators developed a forward-view PAE system with

a 3.2-mm diameter footprint that is capable of imaging the microvascular anatomy at a resolution of tens of micrometres and with an imaging depth of several millimetres<sup>115</sup>. In summary, although such systems are still in their early stages, novel PAI systems have shown potential for image-guided surgical procedures.

**Contrast-enhanced PAI for real-time guidance.** In addition to using endogenous contrast for guidance of surgery, many exogenous contrast agents (typically nanomolecules) have been designed to accumulate at target sites and enhance the photoacoustic signal omitted by the target lesions<sup>176</sup>. Owing to the strong optical absorption (orders of magnitude greater than that of organic dyes) in the NIR range, various gold nanoparticles have been developed for PAI. For example, gold nanoparticles coated with silica that includes Raman and MRI-active layers have been developed for triple modality (PAI–MRI–Raman) imaging for the accurate delineation of brain tumour margins<sup>177</sup> (FIG. 5b). When intravenously injected into glioblastoma-bearing mice, these nanoparticles accumulate and are retained by the tumours without accumulating in the surrounding non-malignant tissues, thus enabling non-invasive tumour delineation through the intact skull.

For faster clinical translation, researchers have also investigated PAI of magnetic iron oxide nanoparticles that have the advantages of being biodegradable and having low levels of toxicity, and have already been used in combination with MRI in patients<sup>178</sup>. PAI of breast cancers targeted using this nanoparticle conjugated with NIR dye-labelled peptide fragments has been reported in a mouse model<sup>179</sup>. Similar to fluorescence imaging, PAI provides high levels of contrast while maintaining similar imaging depths and levels of resolution as those achieved with ultrasonography. Surgeons currently might use ultrasonography to assess the tumour margins during certain forms of central nervous system tumour resection. The integration of PAI could potentially improve both the sensitivity and specificity of this approach, and thus better identify residual lesions. Thus far, no tumour-labelling dye designed for use with PAI has been approved by the FDA, although this imaging modality can in principle detect any FDA-approved chromophores that are optically absorptive<sup>151</sup>. Here, spectroscopic PAI would typically be used to differentiate the contrast agents from the haematogenous background.

### Monitoring drug delivery

Real-time monitoring of pharmacokinetic and pharmacodynamic processes in biological tissues provides important feedback for cancer therapy. In this regard, PAI offers several notable advantages over other imaging modalities in small animal research, particularly for studies requiring high-contrast, high-speed, high-resolution and whole-body imaging of drug delivery<sup>13,180,181</sup>. In clinical practice, however, fewer prescribed drugs strongly absorb NIR light, which is needed to penetrate relatively deeply (>1 cm) into biological tissues. As a result of this lack of NIR absorption, various drug carriers that absorb NIR light have been developed for PAI<sup>176</sup>. Notably, certain contrast agents can also act as photothermal therapy

(PTT) and/or photodynamic therapy (PDT), such as gold nanoparticles<sup>182,183</sup>.

**Nanoscale drug-conjugated carriers.** Various nanoparticles are emerging as useful drug carriers and contrast enhancers for PAI<sup>184–188</sup>. For example, doxorubicin, a drug designed to inhibit the proliferation of human breast cancer cells, can be loaded into fucoidan-capped gold nanoparticles for PAI of anticancer therapy in breast cancer cell lines<sup>185</sup>. Another group developed organic vesicles with a drug release mechanism under laser illumination. This approach enables PAI to be performed using a wider light beam with a lower fluence with intermittent drug release achieved by shrinking the beam width for a higher fluence<sup>186</sup>. Combined with the use of FDA-approved dyes, such as ICG, to enhance light absorbance, drug carriers prescribed for human use can be tracked in vivo using PAI. Although much research and testing remains to be conducted, PAI has the potential to complement PET–CT to enable high-resolution, high-speed, localized imaging, especially in scenarios requiring frequent non-invasive assessments.

**Photothermal and photodynamic agents.** Light-activated, photosensitizer-based therapies have been established as safe modalities for tumour ablation via either localized thermal or chemical damage. PTT usually involves higher laser fluences than PDT (typically 50–100 J/cm<sup>2</sup>)<sup>189</sup>, whereas the illumination required for PAI involves an optical fluence three orders of magnitude lower (typically <100 mJ/cm<sup>2</sup>) than that required for PDT<sup>32</sup>. Similar to PAI, both PTT and PDT are restricted to depths within the optical dissipation limit; therefore, PAI could be used in parallel to provide anatomical, functional and molecular information to guide these two emerging therapeutic fields.

PTT agents have not yet been tested in large-cohort clinical trials. Nonetheless, these agents have several properties that could be implemented for clinical PAI approaches, such as increased photothermal efficiency with lower illumination and the ability to act as perfect PAI contrast agents<sup>190</sup>. Common PTT agents can be classified into five types<sup>189</sup>: organic dye molecules (such as ICG); organic nanoparticles (such as porphyrin–lipid conjugate porphyrins<sup>187</sup>); noble metal materials (particularly gold nanoparticles<sup>182</sup>); carbon-based materials (such as carbon nanotubes<sup>191</sup>); and other inorganic materials (such as quantum dots<sup>192</sup>). For example, cyclic Arg–Gly–Asp (RGD) peptide-conjugated plasmonic gold nanostars (GNS) are designed to specifically target the newly developed tumour vasculature, enabling highly sensitive photoacoustic angiography and PTT. After the administration of RGD–GNS, tumour growth is effectively inhibited by the activation of the PTT using continuous wave laser irradiation<sup>183</sup> (FIG. 5c). In 2019, a phase I trial demonstrated the safety and feasibility of sterile nanoshells with a silica core and gold shell for focal PTT-based tumour ablation in patients with prostate cancer<sup>193</sup>. These nanoparticles can be imaged using a PACT-based endoscope<sup>4</sup>.

Agents capable of acting as PDTs have been used to treat patients with cancer for decades<sup>189</sup>. Common PDT

agents include porphyrin and chlorin or phthalocyanine derivatives, most of which have high photothermal conversion efficiencies<sup>194</sup>. PDT has been applied clinically in patients with cancers of the skin<sup>195</sup>, oesophagus<sup>196</sup>, lung<sup>197</sup> and prostate<sup>198</sup>. Probably owing to limited clinical resources, PAI has not been used to image agents capable of PDT in patients, although several preclinical studies have demonstrated the potential of this approach<sup>199–203</sup>. For example, in an analysis of the performance of five photosensitizers as PAI contrast agents, zinc phthalocyanine (ZnPc) provided the highest photoacoustic signal amplitude<sup>199</sup>. ZnPc was then injected into mice bearing subcutaneous tumours. Using PAI, researchers demonstrated the accumulation of ZnPc over time with the peak tumour to muscle ratio of the photoacoustic signals appearing 1 h after ZnPc injection, thus demonstrating the potential of photosensitizers as PAI contrast agents. In summary, PAI has the potential to image PDT/PTT agents in real time in patients with cancer. By imaging both endogenous (blood concentration and sO<sub>2</sub>) and exogenous contrasts (the PDT/PTT agent), PAI could enable improved therapy monitoring and assessment.

**Radioactive seed localization.** The role of PAI in real-time seed tracking in the context of cancer brachytherapy has also been explored<sup>204–206</sup>. Owing to their tiny size (diameter <1 mm), the seeds filled with isotopes are barely detectable using ultrasonography and are currently located using post-procedural MRI or X-ray CT. For real-time seed deployment, investigators used in vivo PAI to place three brachytherapy seeds coated with black ink into a dog's prostate<sup>204</sup>. The PAI system illuminated the seeds via an optical fibre inserted into a brachytherapy needle and photoacoustic signals were detected using a transrectal ultrasound probe. PAI has the potential to complement whole-body imaging modalities and provide more localized, clearer and faster imaging of the seeds, particularly when the targeted lesion is located within the light dissipation limit<sup>10</sup>.

## Conclusions

Over the past decade<sup>207</sup>, the clinical translation of PAI has accelerated owing to improved access to multi-channel data acquisition modules and customizable large-scale ultrasonic arrays. Multiscale PAI with consistent contrast could have an important role in biomedicine because it provides scalably high levels of spatial resolution and imaging depth and thus enables a holistic understanding of biological functions, from organelles to organs<sup>23</sup>. PAI has shown promise to provide guidance on cancer screening, diagnosis and treatment (FIG. 6). Specifically, PACT has been used successfully to detect breast tumours based on their associated angiogenesis and relative stiffness, has guided the diagnosis of such lesions based on the level of blood oxygen saturation and vascularity, and has been applied to assess treatment responses based on changes in anatomy and function. In early 2021, the first PAI system was approved by the FDA for breast cancer diagnosis<sup>31</sup>. In human skin, PAM and PACT have been applied to delineate skin cancer masses, track circulating cancer cells, and detect melanoma metastases in SLNs. PAE has demonstrated utility

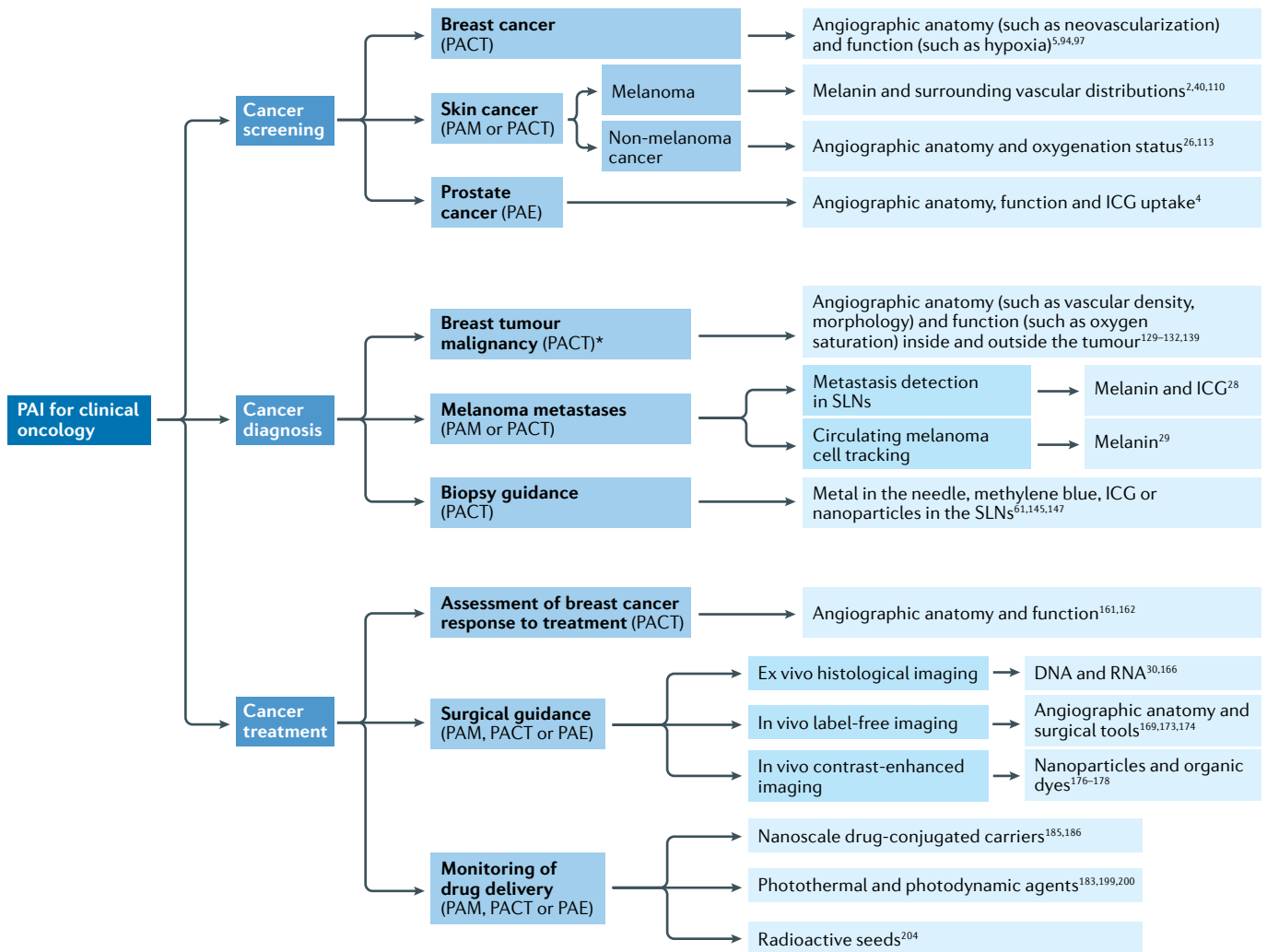


Fig. 6 | **Selection of the PAI configurations and contrasts according to clinical applications.** ICG, indocyanine green; PACT, photoacoustic CT; PAE, photoacoustic endoscopy; PAI, photoacoustic imaging; PAM, photoacoustic microscopy; SLNs, sentinel lymph nodes. \*A hand-held PACT probe has been approved by the FDA for breast cancer diagnosis<sup>31</sup>.

for the detection of prostate cancer and the potential to image other internal organs. PAM has also shown promise as an intraoperative method of assessing cancer margin status, thus avoiding the need for fixation, staining or even sectioning of the excised specimens. Combined with contrast agents, photoacoustic molecular imaging is expected to benefit precision medicine by providing a more precise diagnosis that enables more effective treatment. In summary, PAI has been developed to provide advanced imaging performance and could form the basis of several broad clinical applications. However, long-term and dedicated comparative clinical studies are required to establish the added value of specific applications. Evidence-based integration into clinical workflows is also essential.

From the application perspective, intensive efforts are being made to achieve successful clinical translation. To facilitate cancer screening, the reliability of PAI needs to be improved by standardizing both the technology and its operation. Radiologists are likely to be the early adopters of this technology, and many will require specific training on how to interpret the new information and image

features acquired by PAI systems, which can be naturally integrated with ultrasonography. To benefit cancer diagnosis, more comparative clinical data are required to develop a diagnostic model that clearly improves and can be integrated into the current workflow. Other than direct cancer diagnosis, PAI can also aid existing diagnostic methods (such as core needle biopsy sampling) with the development of custom-designed PAI systems. To aid cancer treatment, PAI can potentially provide feedback on the effects of therapeutic interventions. For example, anti-angiogenesis therapy has been proven to be effective in only a subset of patients with cancer<sup>208</sup>, who might have a similar angiographic anatomy<sup>78</sup>. Therefore, PAI could be used as a prognostic tool and also improve treatment outcomes by enabling timely monitoring. Further clinical translation of these various approaches will require a transition from scattered and small-scale feasibility studies to application-oriented and large-scale, prospective clinical trials designed to identify specific improvements to existing workflows.

Published online: 23 March 2022

1. Lin, L. et al. High-speed three-dimensional photoacoustic computed tomography for preclinical research and clinical translation. *Nat. Commun.* **12**, 882 (2021).
2. Favazza, C. P., Jassim, O., Cornelius, L. A. & Wang, L. H. V. *In vivo* photoacoustic microscopy of human cutaneous microvasculature and a nevus. *J. Biomed. Opt.* **16**, 016015 (2011).
3. Diot, G. et al. Multispectral optoacoustic tomography (MSOT) of human breast cancer. *Clin. Cancer Res.* **23**, 6912–6922 (2017).
4. Kothapalli, S. R. et al. Simultaneous transrectal ultrasound and photoacoustic human prostate imaging. *Sci. Transl. Med.* **11**, eaav2169 (2019).
5. Lin, L. et al. Single-breath-hold photoacoustic computed tomography of the breast. *Nat. Commun.* **9**, 2352 (2018).
6. Lin, L. & Wang, L. H. V. in *Advances in Experimental Medicine and Biology* Vol. 3233 Ch. 8 (eds Wei, X. & Gu, B.) 147–175 (Springer, 2021).
7. Attia, A. B. E. et al. A review of clinical photoacoustic imaging: current and future trends. *Photoacoustics* **16**, 100144 (2019).
8. Steinberg, I. et al. Photoacoustic clinical imaging. *Photoacoustics* **14**, 77–98 (2019).
9. Upputuri, P. K. & Pramanik, M. Recent advances toward preclinical and clinical translation of photoacoustic tomography: a review. *J. Biomed. Opt.* **22**, 041006 (2017).
10. Wang, L. H. V. & Yao, J. J. A practical guide to photoacoustic tomography in the life sciences. *Nat. Methods* **13**, 627–638 (2016).
11. Valluru, K. S., Wilson, K. E. & Willmann, J. K. Photoacoustic imaging in oncology: translational preclinical and early clinical experience. *Radiology* **280**, 332–349 (2016).
12. Li, L. et al. Single-impulse panoramic photoacoustic computed tomography of small-animal whole-body dynamics at high spatiotemporal resolution. *Nat. Biomed. Eng.* **1**, 0071 (2017).
13. Gargiulo, S., Albanese, S. & Mancini, M. State-of-the-art preclinical photoacoustic imaging in oncology: recent advances in cancer theranostics. *Contrast. Media. Mol. Imaging* **2019**, 5080267 (2019).
14. Dean-Ben, X. L. & Razansky, D. Optoacoustic imaging of the skin. *Exp. Dermatol.* **30**, 1598–1609 (2021).
15. Regensburger, A. P., Wagner, A. L., Claussen, J., Waldner, M. J. & Knieling, F. Shedding light on pediatric diseases: multispectral optoacoustic tomography at the doorway to clinical applications. *Mol. Cell. Pediatr.* **7**, 1–6 (2020).
16. Ravina, K. et al. Prospects of photo- and thermoacoustic imaging in neurosurgery. *Neurosurgery* **87**, 11–24 (2020).
17. Wang, Y. et al. Preclinical evaluation of photoacoustic imaging as a novel noninvasive approach to detect an orthopaedic implant infection. *J. Am. Acad. Orthop. Surg.* **25**, S7–S12 (2017).
18. Zhang, J., Duan, F., Liu, Y. & Nie, L. High-resolution photoacoustic tomography for early-stage cancer detection and its clinical translation. *Radiol. Imaging Cancer* **2**, e190030 (2020).
19. Valluru, K. S. & Willmann, J. K. Clinical photoacoustic imaging of cancer. *Ultrasonography* **35**, 267–280 (2016).
20. Taruttis, A., van Dam, G. M. & Ntziachristos, V. Mesoscopic and macroscopic optoacoustic imaging of cancer. *Cancer Res.* **75**, 1548–1559 (2015).
21. Mehrmohammadi, M., Yoon, S. J., Yeager, D. & Emelianov, S. Y. Photoacoustic imaging for cancer detection and staging. *Curr. Mol. Imaging* **2**, 89–105 (2013).
22. Xia, J., Yao, J. J. & Wang, L. V. Photoacoustic tomography: principles and advances. *Prog. Electromagn. Res.* **147**, 1–22 (2014).
23. Wang, L. H. V. & Hu, S. Photoacoustic tomography: in vivo imaging from organelles to organs. *Science* **335**, 1458–1462 (2012).
24. Rao, A. P., Bokde, N. & Sinha, S. Photoacoustic imaging for management of breast cancer: a literature review and future perspectives. *Appl. Sci. Basel* **10**, 767 (2020).
25. Nyayapathi, N. & Xia, J. Photoacoustic imaging of breast cancer: a mini review of system design and image features. *J. Biomed. Opt.* **24**, 121911 (2019).
26. Attia, A. B. E. et al. Noninvasive real-time characterization of non-melanoma skin cancers with handheld optoacoustic probes. *Photoacoustics* **7**, 20–26 (2017).
27. Li, D., Humayun, L., Vienneau, E., Vu, T. & Yao, J. Seeing through the skin: photoacoustic tomography of skin vasculature and beyond. *JID Innov.* **1**, 100039 (2021).
28. Stoffels, I. et al. Metastatic status of sentinel lymph nodes in melanoma determined noninvasively with multispectral optoacoustic imaging. *Sci. Transl. Med.* **7**, 317ra199 (2015).
29. Hai, P. et al. Label-free high-throughput photoacoustic tomography of suspected circulating melanoma tumor cells in patients *in vivo*. *J. Biomed. Opt.* **25**, 1–17 (2020).
30. Wong, T. T. W. et al. Fast label-free multilayered histology-like imaging of human breast cancer by photoacoustic microscopy. *Sci. Adv.* **3**, e1602168 (2017).
31. Food and Drug Administration. Premarket Approval: Imagio Breast Imaging System (FDA, 2021).
32. Laser Institute of America. ANSI Z136.1–2007: American National Standard for Safe Use of Lasers (LIA, 2007).
33. Yao, J. J. & Wang, L. H. V. Photoacoustic microscopy. *Laser Photonics Rev.* **7**, 758–778 (2013).
34. Xu, M. H. & Wang, L. H. V. Universal back-projection algorithm for photoacoustic computed tomography. *Phys. Rev. E Stat. Nonlin. Soft Matter Phys.* **71**, 016706 (2005).
35. Guo, H., Li, Y., Qi, W. Z. & Xi, L. Photoacoustic endoscopy: a progress review. *J. Biophotonics* **13**, e202000217 (2020).
36. Yao, J. J. & Wang, L. H. V. Photoacoustic tomography: fundamentals, advances and prospects. *Contrast Media Mol. Imaging* **6**, 332–345 (2011).
37. Yao, J. et al. High-speed label-free functional photoacoustic microscopy of mouse brain in action. *Nat. Methods* **12**, 407–410 (2015).
38. Lan, B. et al. High-speed widefield photoacoustic microscopy of small-animal hemodynamics. *Biomed. Opt. Express* **9**, 4689–4701 (2018).
39. Lin, L. et al. High-speed photoacoustic microscopy of mouse cortical microhemodynamics. *J. Biophotonics* **10**, 792–798 (2017).
40. Park, K. et al. Handheld photoacoustic microscopy probe. *Sci. Rep.* **7**, 13359 (2017).
41. Lin, L. et al. Handheld optical-resolution photoacoustic microscopy. *J. Biomed. Opt.* **22**, 41002 (2017).
42. Na, S. et al. Massively parallel functional photoacoustic computed tomography of the human brain. *Nat. Biomed. Eng.* <https://doi.org/10.1038/s41551-021-00735-8> (2021).
43. Weber, J., Beard, P. C. & Bohniek, S. E. Contrast agents for molecular photoacoustic imaging. *Nat. Methods* **13**, 639–650 (2016).
44. Upputuri, P. K. & Pramanik, M. Recent advances in photoacoustic contrast agents for *in vivo* imaging. *Wires Nanomed. Nanobi.* **12**, e1618 (2020).
45. Li, M. C., Tang, Y. Q. & Yao, J. J. Photoacoustic tomography of blood oxygenation: a mini review. *Photoacoustics* **10**, 65–73 (2018).
46. Folkman, J. Role of angiogenesis in tumor growth and metastasis. *Semin. Oncol.* **29**, 15–18 (2002).
47. Weidner, N., Semple, J. P., Welch, W. R. & Folkman, J. Tumor angiogenesis and metastasis—correlation in invasive breast-carcinoma. *N. Engl. J. Med.* **324**, 1–8 (1991).
48. Hanahan, D. & Weinberg, R. A. Hallmarks of cancer: the next generation. *Cell* **144**, 646–674 (2011).
49. Shi, J. H. et al. High-resolution, high-contrast mid-infrared imaging of fresh biological samples with ultraviolet-localized photoacoustic microscopy. *Nat. Photonics* **13**, 609–615 (2019).
50. Zhang, H. F., Maslov, K., Stoica, G. & Wang, L. H. V. Functional photoacoustic microscopy for high-resolution and noninvasive *in vivo* imaging. *Nat. Biotechnol.* **24**, 848–851 (2006).
51. Yao, J. J. & Wang, L. H. V. Recent progress in photoacoustic molecular imaging. *Curr. Opin. Chem. Biol.* **45**, 104–112 (2018).
52. Collins, J. A., Rudenski, A., Gibson, J., Howard, L. & O’Driscoll, R. Relating oxygen partial pressure, saturation and content: the haemoglobin-oxygen dissociation curve. *Breathe* **11**, 195–201 (2015).
53. Grosenick, D., Rinneberg, H., Cubeddu, R. & Taroni, P. Review of optical breast imaging and spectroscopy. *J. Biomed. Opt.* **21**, 091311 (2016).
54. Shah, J. et al. Photoacoustic imaging and temperature measurement for photothermal cancer therapy. *J. Biomed. Opt.* **13**, 034024 (2008).
55. Yao, J. J., Maslov, K. I., Zhang, Y., Xia, Y. N. & Wang, L. V. Label-free oxygen-metabolic photoacoustic microscopy *in vivo*. *J. Biomed. Opt.* **16**, 076003 (2011).
56. Jiang, Y. & Zemp, R. Estimation of cerebral metabolic rate of oxygen consumption using combined multiwavelength photoacoustic microscopy and Doppler microultrasound. *J. Biomed. Opt.* **23**, 016009 (2018).
57. Singh, P. et al. Gold nanoparticles in diagnostics and therapeutics for human cancer. *Int. J. Mol. Sci.* **19**, 1979 (2018).
58. Li, W. W. & Chen, X. Y. Gold nanoparticles for photoacoustic imaging. *Nanomedicine* **10**, 299–320 (2015).
59. Okumura, K. et al. Photoacoustic imaging of tumour vascular permeability with indocyanine green in a mouse model. *Eur. Radiol. Exp.* **2**, 5 (2018).
60. Garcia-Urbe, A. et al. Dual-modality photoacoustic and ultrasound imaging system for noninvasive sentinel lymph node detection in patients with breast cancer. *Sci. Rep.* **5**, 15748 (2015).
61. Forbrich, A., Heinmiller, A. & Zemp, R. J. Photoacoustic imaging of lymphatic pumping. *J. Biomed. Opt.* **22**, 1–6 (2017).
62. Toi, M. et al. Visualization of tumor-related blood vessels in human breast by photoacoustic imaging system with a hemispherical detector array. *Sci. Rep.* **7**, 41970 (2017).
63. Dumani, D. S. et al. in *Proceedings of SPIE. Vol. 10494: Photons Plus Ultrasound: Imaging and Sensing 2018* (eds Oraevsky, A. A. & Wang, L. V.) 10494-2W (SPIE, 2018).
64. Hosseinaee, Z., Simmons, J. A. T. & Reza, P. H. Dual-modal photoacoustic imaging and optical coherence tomography [review]. *Front. Phys.* **8**, 635 (2021).
65. Park, J. et al. Quadruple ultrasound, photoacoustic, optical coherence, and fluorescence fusion imaging with a transparent ultrasound transducer. *Proc. Natl Acad. Sci. USA* **118**, e1920879118 (2021).
66. Song, W. et al. Fully integrated reflection-mode photoacoustic, two-photon, and second harmonic generation microscopy *in vivo*. *Sci. Rep.* **6**, 32240 (2016).
67. Rao, B., Soto, F., Kerschensteiner, D. & Wang, L. H. V. Integrated photoacoustic, confocal, and two-photon microscope. *J. Biomed. Opt.* **19**, 36002 (2014).
68. Fass, L. Imaging and cancer: a review. *Mol. Oncol.* **2**, 115–152 (2008).
69. Ariztia, E. V., Lee, C. J., Gogoi, R. & Fishman, D. A. The tumor microenvironment: key to early detection. *Crit. Rev. Clin. Lab. Sci.* **43**, 393–425 (2006).
70. Muz, B., de la Puente, P., Azab, F. & Azab, A. K. The role of hypoxia in cancer progression, angiogenesis, metastasis, and resistance to therapy. *Hypoxia* **3**, 83–92 (2015).
71. Hockel, M. & Vaupel, P. Tumor hypoxia: definitions and current clinical, biologic, and molecular aspects. *J. Natl Cancer Inst.* **93**, 266–276 (2001).
72. von Euler-Chelpin, M., Lillholm, M., Vejborg, I., Nielsen, M. & Lyng, E. Sensitivity of screening mammography by density and texture: a cohort study from a population-based screening program in Denmark. *Breast Cancer Res.* **21**, 111 (2019).
73. Devolli-Disha, E., Manxhuka-Kerliu, S., Ymeri, H. & Kutllovci, A. Comparative accuracy of mammography and ultrasound in women with breast symptoms according to age and breast density. *Bosn. J. Basic. Med.* **9**, 131–136 (2009).
74. Moss, S., Faulkner, K., Law, J. & Young, K. Benefits versus risks from mammography—a critical reassessment. *Cancer* **79**, 628–628 (1997).
75. Sim, L. S. J., Hendriks, J. H. C. L. & Fook-Chong, S. M. C. Breast ultrasound in women with familial risk of breast cancer. *Ann. Acad. Med. Singap.* **33**, 600–606 (2004).
76. Boudreau, N. & Myers, C. Breast cancer-induced angiogenesis: multiple mechanisms and the role of the microenvironment. *Breast Cancer Res.* **5**, 140–146 (2003).
77. Folkman, J. Angiogenesis in cancer, vascular, rheumatoid and other disease. *Nat. Med.* **1**, 27–31 (1995).
78. Banerjee, S., Dowsett, M., Ashworth, A. & Martin, L. A. Mechanisms of disease: angiogenesis and the management of breast cancer. *Nat. Clin. Pract. Oncol.* **4**, 536–550 (2007).
79. Pavlakis, K. et al. The assessment of angiogenesis and fibroblastic stromagenesis in hyperplastic and pre-invasive breast lesions. *BMC Cancer* **8**, 88 (2008).
80. Vogl, G., Dietze, O. & Hauser-Kronberger, C. Angiogenic potential of ductal carcinoma in situ (DCIS) of human breast. *Histopathology* **47**, 617–624 (2005).
81. Viacava, P. et al. Angiogenesis and VEGF expression in pre-invasive lesions of the human breast. *J. Pathol.* **204**, 140–146 (2004).

82. Cao, Y., Paner, G. P., Kahn, L. B. & Rajan, P. B. Noninvasive carcinoma of the breast—angiogenesis and cell proliferation. *Arch. Pathol. Lab. Med.* **128**, 893–896 (2004).
83. Teo, N. B. et al. Vascular density and phenotype around ductal carcinoma in situ (DCIS) of the breast. *Br. J. Cancer* **86**, 905–911 (2002).
84. Heffelfinger, S. C., Miller, M. A., Yassin, R. & Gear, R. Angiogenic growth factors in preinvasive breast disease. *Clin. Cancer Res.* **5**, 2867–2876 (1999).
85. Heffelfinger, S. C., Yassin, R., Miller, M. A. & Lower, E. Vascularity of proliferative breast disease and carcinoma in situ correlates with histological features. *Clin. Cancer Res.* **2**, 1873–1878 (1996).
86. Carpenter, P. M., Chen, W. P., Mendez, A., McLaren, C. E. & Su, M. Y. Angiogenesis in the progression of breast ductal proliferations. *Int. J. Surg. Pathol.* **19**, 335–341 (2011).
87. Bluff, J. E. et al. Angiogenesis is associated with the onset of hyperplasia in human ductal breast disease. *Br. J. Cancer* **101**, 666–672 (2009).
88. Nagy, J. A., Chang, S. H., Dvorak, A. M. & Dvorak, H. F. Why are tumour blood vessels abnormal and why is it important to know? *Br. J. Cancer* **100**, 865–869 (2009).
89. Gordon, M. S., Mendelson, D. S. & Kato, G. Tumor angiogenesis and novel antiangiogenic strategies. *Int. J. Cancer* **126**, 1777–1787 (2010).
90. Madu, C. O., Wang, S., Madu, C. O. & Lu, Y. Angiogenesis in breast cancer progression, diagnosis, and treatment. *J. Cancer* **11**, 4474–4494 (2020).
91. Manohar, S. & Dantuma, M. Current and future trends in photoacoustic breast imaging. *Photoacoustics* **16**, 100134 (2019).
92. Zhang, G. J., Li, W. Z., Yang, M. & Li, C. H. Developing a photoacoustic whole-breast imaging system based on the synthetic matrix array. *Front. Phys.* <https://doi.org/10.3389/fphy.2020.600589> (2020).
93. Nyayapathi, N. et al. Dual scan mammoscope (DSM)—a new portable photoacoustic breast imaging system with scanning in craniocaudal plane. *IEEE Trans. Biomed. Eng.* **67**, 1321–1327 (2020).
94. Heijblom, M. et al. The state of the art in breast imaging using the Twente photoacoustic mammoscope: results from 31 measurements on malignancies. *Eur. Radiol.* **26**, 3874–3887 (2016).
95. Schoustra, S. M. et al. Twente photoacoustic mammoscope 2: system overview and three-dimensional vascular network images in healthy breasts. *J. Biomed. Opt.* **24**, 1–12 (2019).
96. Oraevsky, A. et al. in *Proceedings of SPIE, Vol. 10494: Photons Plus Ultrasound: Imaging and Sensing 2018* (eds Oraevsky, A. A. & Wang, L. V.) 10494 2Y (SPIE, 2018).
97. Matsumoto, Y. et al. Visualising peripheral arterioles and venules through high-resolution and large-area photoacoustic imaging. *Sci. Rep.* **8**, 14930 (2018).
98. Hu, P., Li, L., Lin, L. & Wang, L. H. V. Spatiotemporal anti-aliasing in photoacoustic computed tomography. *IEEE Trans. Med. Imaging* **39**, 3535–3547 (2020).
99. Bohndiek, S. Addressing photoacoustics standards. *Nat. Photonics* **13**, 298–298 (2019).
100. Kaplan, S. S. Automated whole breast ultrasound. *Radiol. Clin. North Am.* **52**, 539–546 (2014).
101. Leong, L. C., Gogna, A., Pant, R., Ng, F. C. & Sim, L. S. Supplementary breast ultrasound screening in Asian women with negative but dense mammograms—a pilot study. *Ann. Acad. Med. Singap.* **41**, 432–439 (2012).
102. Rhodes, A. R. Public-education and cancer of the skin—What do people need to know about melanoma and non-melanoma skin-cancer. *Cancer* **75**, 613–636 (1995).
103. Lutz, K., Hayward, V., Joseph, M., Wong, E. & Temple-Oberle, C. Current biopsy practices for suspected melanoma: a survey of family physicians in Southwestern Ontario. *Plast. Surg.* **22**, 175–178 (2014).
104. Dummer, W. et al. Preoperative characterization of pigmented skin lesions by epiluminescence microscopy and high-frequency ultrasound. *Arch. Dermatol.* **131**, 279–285 (1995).
105. Hult, J. et al. Comparison of photoacoustic imaging and histopathological examination in determining the dimensions of 52 human melanomas and nevi ex vivo. *Biomed. Opt. Express* **12**, 4097–4114 (2021).
106. von Knorring, T. & Mogensen, M. Photoacoustic tomography for assessment and quantification of cutaneous and metastatic malignant melanoma—a systematic review. *Photodiagnosis Photodyn. Ther.* **33**, 102095 (2021).
107. Aguirre, J. et al. Precision assessment of label-free psoriasis biomarkers with ultra-broadband photoacoustic mesoscopy. *Nat. Biomed. Eng.* **1**, 0068 (2017).
108. Nagae, K. et al. Real-time 3D photoacoustic visualization system with a wide field of view for imaging human limbs. *F1000Res* **7**, 1813 (2018).
109. Brown, E., Brunker, J. & Bohndiek, S. E. Photoacoustic imaging as a tool to probe the tumour microenvironment. *Dis. Model Mech.* <https://doi.org/10.1242/dmm.039636> (2019).
110. Brethnach, A. et al. Preoperative measurement of cutaneous melanoma and nevi thickness with photoacoustic imaging. *J. Med. Imaging* **5**, 015004 (2018).
111. Plumb, A. A., Huynh, N. T., Guggenheim, J., Zhang, E. & Beard, P. Rapid volumetric photoacoustic tomographic imaging with a Fabry-Perot ultrasound sensor depicts peripheral arteries and microvascular vasomotor responses to thermal stimuli. *Eur. Radiol.* **28**, 1037–1045 (2018).
112. Jathoul, A. P. et al. Deep *in vivo* photoacoustic imaging of mammalian tissues using a tyrosinase-based genetic reporter. *Nat. Photonics* **9**, 239–246 (2015).
113. Chen, Z. et al. Non-invasive multimodal optical coherence and photoacoustic tomography for human skin imaging. *Sci. Rep.* **7**, 17975 (2017).
114. Catalona, W. J., Smith, D. S., Ratliff, T. L. & Basler, J. W. Detection of organ-confined prostate-cancer is increased through prostate-specific antigen-based screening. *JAMA* **270**, 948–954 (1993).
115. Ansari, R., Zhang, E. Z., Desjardins, A. E. & Beard, P. C. All-optical forward-viewing photoacoustic probe for high-resolution 3D endoscopy. *Light Sci. Appl.* **7**, 75 (2018).
116. Li, Y., Lu, G. X., Zhou, Q. F. & Chen, Z. P. Advances in endoscopic photoacoustic imaging. *Photonics* **8**, 281 (2021).
117. Basij, M. et al. Miniaturized phased-array ultrasound and photoacoustic endoscopic imaging system. *Photoacoustics* **15**, 100139 (2019).
118. Dangi, A. et al. in *Proceedings of SPIE, Vol. 10878: Photons Plus Ultrasound: Imaging and Sensing 2019* (eds Oraevsky, A. A. & Wang, L. V.) (SPIE, 2019).
119. Yang, G. et al. Co-registered photoacoustic and ultrasound imaging of human colorectal cancer. *J. Biomed. Opt.* **24**, 1–13 (2019).
120. Yang, J. M. et al. Three-dimensional photoacoustic endoscopic imaging of the rabbit esophagus. *PLoS ONE* **10**, e0120269 (2015).
121. Yang, M. et al. Photoacoustic/ultrasound dual imaging of human thyroid cancers: an initial clinical study. *Biomed. Opt. Express* **8**, 3449–3457 (2017).
122. Salehi, H. S. et al. Coregistered photoacoustic and ultrasound imaging and classification of ovarian cancer: *ex vivo* and *in vivo* studies. *J. Biomed. Opt.* **21**, 46006 (2016).
123. Nandy, S. et al. Evaluation of ovarian cancer: initial application of coregistered photoacoustic tomography and US. *Radiology* **289**, 740–747 (2018).
124. Yan, Y. et al. Spectroscopic photoacoustic imaging of cervical tissue composition in excised human samples. *PLoS ONE* **16**, e0247385 (2021).
125. Dogra, V. S. et al. Preliminary results of *ex vivo* multispectral photoacoustic imaging in the management of thyroid cancer. *Am. J. Roentgenol.* **202**, W552–W558 (2014).
126. Mitrayana, Apriyanto, D. K. & Satriawan, M. CO<sub>2</sub> laser photoacoustic spectrometer for measuring acetone in the breath of lung cancer patients. *Biosensors* **10**, 55 (2020).
127. Butler, R. et al. Photoacoustic breast imaging: imaging-pathology correlation of photoacoustic features in benign and malignant breast masses. *Am. J. Roentgenol.* **211**, 1155–1170 (2018).
128. de Heer, E. C., Jalving, M. & Harris, A. L. HIFs, angiogenesis, and metabolism: elusive enemies in breast cancer. *J. Clin. Invest.* **130**, 5074–5087 (2020).
129. Oraevsky, A. A. et al. Clinical photoacoustic imaging combined with ultrasound for coregistered functional and anatomical mapping of breast tumors. *Photoacoustics* **12**, 30–45 (2018).
130. Neuschler, E. I. et al. A pivotal study of photoacoustic imaging to diagnose benign and malignant breast masses: a new evaluation tool for radiologists. *Radiology* **287**, 398–412 (2018).
131. Menezes, G. L. G. et al. Downgrading of breast masses suspicious for cancer by using photoacoustic breast imaging. *Radiology* **288**, 355–365 (2018).
132. Dogan, B. E. et al. Photoacoustic imaging and gray-scale US features of breast cancers: correlation with molecular subtypes. *Radiology* **292**, 564–572 (2019).
133. Food and Drug Administration. Summary of safety and effectiveness data (SSED): Imagio® breast imaging system. [https://www.accessdata.fda.gov/cdrh\\_docs/pdf20/P200003B.pdf](https://www.accessdata.fda.gov/cdrh_docs/pdf20/P200003B.pdf) (2021).
134. Xu, Y., Wang, L. V., Ambartsoumian, G. & Kuchment, P. Reconstructions in limited-view thermoacoustic tomography. *Med. Phys.* **31**, 724–733 (2004).
135. Li, G. et al. Tripling the detection view of high-frequency linear-array-based photoacoustic computed tomography by using two planar acoustic reflectors. *Quant. Imaging Med. Surg.* **5**, 57–62 (2015).
136. Zhang, R. et al. Exploring the diagnostic value of photoacoustic imaging for breast cancer: the identification of regional photoacoustic signal differences of breast tumors. *Biomed. Opt. Express* **12**, 1407–1421 (2021).
137. Zalev, J. et al. Opto-acoustic imaging of relative blood oxygen saturation and total hemoglobin for breast cancer diagnosis. *J. Biomed. Opt.* **24**, 121915 (2019).
138. Fakhrejahani, E. et al. Clinical report on the first prototype of a photoacoustic tomography system with dual illumination for breast cancer imaging. *PLoS ONE* **10**, e0139113 (2015).
139. Yang, M. et al. Quantitative analysis of breast tumours aided by three-dimensional photoacoustic/ultrasound functional imaging. *Sci. Rep.* **10**, 8047 (2020).
140. Neal, L. et al. Diagnosis and management of benign, atypical, and indeterminate breast lesions detected on core needle biopsy. *Mayo Clin. Proc.* **89**, 536–547 (2014).
141. Faries, M. B. et al. Lymph node metastasis in melanoma: a debate on the significance of nodal metastases, conditional survival analysis and clinical trials. *Clin. Exp. Metastas.* **35**, 431–442 (2018).
142. He, Y. et al. *In vivo* label-free photoacoustic flow cytography and on-the-spot laser killing of single circulating melanoma cells. *Sci. Rep.* **6**, 39616 (2016).
143. Vogl, T. & Bisdas, S. Lymph node staging. *Top. Magn. Reson. Imaging* **18**, 303–316 (2007).
144. Hsueh, E. C., Hansen, N. & Giuliano, A. E. Intraoperative lymphatic mapping and sentinel lymph node dissection in breast cancer. *Cancer J. Clin.* **50**, 279–291 (2000).
145. Liu, S. D. et al. *In vivo* photoacoustic sentinel lymph node imaging using clinically-approved carbon nanoparticles. *IEEE Trans. Biomed. Eng.* **67**, 2033–2042 (2020).
146. Kim, C. et al. Handheld array-based photoacoustic probe for guiding needle biopsy of sentinel lymph nodes. *J. Biomed. Opt.* **15**, 046010 (2010).
147. Kang, J. et al. Real-time sentinel lymph node biopsy guidance using combined ultrasound, photoacoustic, fluorescence imaging: *in vivo* proof-of-principle and validation with nodal obstruction. *Sci. Rep.* **7**, 45008 (2017).
148. Wang, H. et al. Three-dimensional interventional photoacoustic imaging for biopsy needle guidance with a linear array transducer. *J. Biophotonics* **12**, e201900212 (2019).
149. Piras, D., Grijsen, C., Schutte, P., Steenberg, W. & Manohar, S. Photoacoustic needle: minimally invasive guidance to biopsy. *J. Biomed. Opt.* **18**, 070502 (2013).
150. Chen, Z. Y. et al. Advance of molecular imaging technology and targeted imaging agent in imaging and therapy. *Biomed. Res. Int.* **2014**, 19324 (2014).
151. National Center for Biotechnology Information. Molecular imaging and contrast agent database (MICAD) (National Center for Biotechnology Information, 2004–2013).
152. Tummers, W. S. et al. Intraoperative pancreatic cancer detection using tumor-specific multimodality molecular imaging. *Ann. Surg. Oncol.* **25**, 1880–1888 (2018).
153. Sano, K. et al. *In vivo* photoacoustic imaging of cancer using indocyanine green-labeled monoclonal antibody targeting the epidermal growth factor receptor. *Biochem. Biophys. Res. Commun.* **464**, 820–825 (2015).
154. Giusti, R. M., Shastri, K. A., Cohen, M. H., Keegan, P. & Pazdur, R. FDA drug approval summary: Panitumumab (Vectibix). *Oncologist* **12**, 577–583 (2007).
155. Cong, F., Yu, H. & Gao, X. Expression of CD24 and B7-H3 in breast cancer and the clinical significance. *Oncol. Lett.* **14**, 7185–7190 (2017).

156. Wilson, K. E. et al. Spectroscopic photoacoustic molecular imaging of breast cancer using a B7-H3-targeted ICG contrast agent. *Theranostics* **7**, 1463–1476 (2017).
157. Korde, L. A. et al. Neoadjuvant chemotherapy, endocrine therapy, and targeted therapy for breast cancer: ASCO guideline. *J. Clin. Oncol.* **39**, 1485–1505 (2021).
158. Davidson, N. E. & Morrow, M. Sometimes a great notion—an assessment of neoadjuvant systemic therapy for breast cancer. *J. Natl Cancer J* **197**, 159–161 (2005).
159. Cortazar, P. & Kluetz, P. C. Neoadjuvant breast cancer therapy and drug development. *Clin. Adv. Hematol. Oncol.* **13**, 755–761 (2015).
160. Cocconi, G. et al. Problems in evaluating response of primary breast-cancer to systemic therapy. *Breast Cancer Res. Treat.* **4**, 309–313 (1984).
161. Lin, L. et al. Photoacoustic computed tomography of breast cancer in response to neoadjuvant chemotherapy. *Adv. Sci.* **8**, 2003396 (2021).
162. Li, X. et al. Functional photoacoustic tomography of breast cancer: pilot clinical results. *Biomed. Opt. Express* **10**, 1364/B10MED.2014.B53A.63 (2014).
163. Wiacek, A. & Bell, M. A. L. Photoacoustic-guided surgery from head to toe [invited]. *Biomed. Opt. Express* **12**, 2079–2117 (2021).
164. Moran, M. S. et al. Society of Surgical Oncology–American Society for Radiation Oncology consensus guideline on margins for breast-conserving surgery with whole-breast irradiation in stages I and II invasive breast cancer. *J. Clin. Oncol.* **32**, 1507–1515 (2014).
165. Yao, D. K., Maslov, K., Shung, K. K., Zhou, Q. F. & Wang, L. V. *In vivo* label-free photoacoustic microscopy of cell nuclei by excitation of DNA and RNA. *Opt. Lett.* **35**, 4139–4141 (2010).
166. Imai, T. et al. High-throughput ultraviolet photoacoustic microscopy with multifocal excitation. *J. Biomed. Opt.* **23**, 1–6 (2018).
167. Kim, G. R. et al. Photoacoustic imaging of breast microcalcifications: a preliminary study with 8-gauge core-biopsied breast specimens. *PLoS ONE* **9**, e105878 (2014).
168. Asgari, S., Röhrborn, H.-J., Engelhorn, T., Fauser, B. & Stolke, D. Intraoperative measurement of cortical oxygen saturation and blood volume adjacent to cerebral arteriovenous malformations using near-infrared spectroscopy. *Neurosurgery* **52**, 1298–1306 (2003).
169. Moradi, H., Tang, S. & Salcudean, S. E. Toward robot-assisted photoacoustic imaging: implementation using the da Vinci research kit and virtual fixtures. *IEEE Robot. Autom. Lett.* **4**, 1807–1814 (2019).
170. Gandhi, N., Allard, M., Kim, S., Kazanzides, P. & Bell, M. A. L. Photoacoustic-based approach to surgical guidance performed with and without a da Vinci robot. *J. Biomed. Opt.* **22**, 121606 (2017).
171. Gilmour, D. T., Das, S. & Flowerdew, G. Rates of urinary tract injury from gynecologic surgery and the role of intraoperative cystoscopy. *Obstet. Gynecol.* **107**, 1366–1372 (2006).
172. Delacroix, S. E. & Winters, J. Urinary tract injuries: recognition and management. *Clin. Colon. Rectal Surg.* **23**, 104–112 (2010).
173. Allard, M., Shubert, J. & Bell, M. A. L. Feasibility of photoacoustic-guided teleoperated hysterectomies. *J. Med. Imaging* **5**, 021213 (2018).
174. Bell, M. A. L., Ostrowski, A. K., Li, K., Kazanzides, P. & Boctor, E. M. Localization of transcranial targets for photoacoustic-guided endonasal surgeries. *Photoacoustics* **3**, 78–87 (2015).
175. Graham, M. T., Huang, J. Q., Creighton, F. X. & Bell, M. A. L. Simulations and human cadaver head studies to identify optimal acoustic receiver locations for minimally invasive photoacoustic-guided neurosurgery. *Photoacoustics* **19**, 100183 (2020).
176. Moore, C. & Jocker, J. V. Strategies for image-guided therapy, surgery, and drug delivery using photoacoustic imaging. *Theranostics* **9**, 1550–1571 (2019).
177. Kircher, M. F. et al. A brain tumor molecular imaging strategy using a new triple-modality MRI-photoacoustic-Raman nanoparticle. *Nat. Med.* **18**, 829–834 (2012).
178. Grootendorst, D. J. et al. Evaluation of superparamagnetic iron oxide nanoparticles (Endorem (R)) as a photoacoustic contrast agent for intra-operative nodal staging. *Contrast Media Mol. Imaging* **8**, 83–91 (2013).
179. Xi, L. et al. Photoacoustic and fluorescence image-guided surgery using a multifunctional targeted nanoprobe. *Ann. Surg. Oncol.* **21**, 1602–1609 (2014).
180. Zhang, Y. Q., Yu, J. C., Kahkoska, A. R. & Gu, Z. Photoacoustic drug delivery. *Sensors* **17**, 1400 (2017).
181. Wu, Z. G. et al. A microbotic system guided by photoacoustic computed tomography for targeted navigation in intestines *in vivo*. *Sci. Robot* **4**, eaax0613 (2019).
182. Huang, X. H., El-Sayed, I. H., Qian, W. & El-Sayed, M. A. Cancer cell imaging and photothermal therapy in the near-infrared region by using gold nanorods. *J. Am. Chem. Soc.* **128**, 2115–2120 (2006).
183. Nie, L. M. et al. *In vivo* volumetric photoacoustic molecular angiography and therapeutic monitoring with targeted plasmonic nanostars. *Small* **10**, 1585–1593 (2014).
184. Moon, G. D. et al. A new theranostic system based on gold nanocages and phase-change materials with unique features for photoacoustic imaging and controlled release. *J. Am. Chem. Soc.* **133**, 4762–4765 (2011).
185. Manivasagan, P. et al. Doxorubicin-loaded fucoidan capped gold nanoparticles for drug delivery and photoacoustic imaging. *Int. J. Biol. Macromol.* **91**, 578–588 (2016).
186. Zhong, J. P., Yang, S. H., Wen, L. W. & Xing, D. Imaging-guided photoacoustic drug release and synergistic chemo-photoacoustic therapy with paclitaxel-containing nanoparticles. *J. Control. Rel.* **226**, 77–87 (2016).
187. Lovell, J. F. et al. Porphyrinsomes nanovesicles generated by porphyrin bilayers for use as multimodal biophotonic contrast agents. *Nat. Mater.* **10**, 324–332 (2011).
188. Hannah, A., Luke, G., Wilson, K., Homan, K. & Emelianov, S. Indocyanine green-loaded photoacoustic nanodroplets: dual contrast nanoconstructs for enhanced photoacoustic and ultrasound imaging. *ACS Nano* **8**, 250–259 (2014).
189. Li, X. S., Lovell, J. F., Yoon, J. & Chen, X. Y. Clinical development and potential of photothermal and photodynamic therapies for cancer. *Nat. Rev. Clin. Oncol.* **17**, 657–674 (2020).
190. Liu, Y. J., Bhattarai, P., Dai, Z. F. & Chen, X. Y. Photothermal therapy and photoacoustic imaging via nanotheranostics in fighting cancer. *Chem. Soc. Rev.* **48**, 2053–2108 (2019).
191. De La Zerde, A. et al. Carbon nanotubes as photoacoustic molecular imaging agents in living mice. *Nat. Nanotechnol.* **3**, 557–562 (2008).
192. Shashkov, E. V., Everts, M., Galanzha, E. I. & Zharov, V. P. Quantum dots as multimodal photoacoustic and photothermal contrast agents. *Nano Lett.* **8**, 3953–3958 (2008).
193. Rastinehad, A. R. et al. Gold nanoshell-localized photothermal ablation of prostate tumors in a clinical pilot device study. *Proc. Natl Acad. Sci. USA* **116**, 18590–18596 (2019).
194. Sharman, W. M., Allen, C. M. & van Lier, J. E. Photodynamic therapeutics: basic principles and clinical applications. *Drug Discov. Today* **4**, 507–517 (1999).
195. Wan, M. T. & Lin, J. Y. Current evidence and applications of photodynamic therapy in dermatology. *Clin. Cosmet. Invest. Dermatol.* **7**, 145 (2014).
196. Qumseya, B. J., David, W. & Wolfson, H. C. Photodynamic therapy for Barrett's esophagus and esophageal carcinoma. *Clin. Endosc.* **46**, 30 (2013).
197. Simone, C. B. II & Cengel, K. A. Photodynamic therapy for lung cancer and malignant pleural mesothelioma. *Semin. Oncol.* **41**, 820–830 (2014).
198. Gheewala, T., Skwor, T. & Munirathinam, G. Photosensitizers in prostate cancer therapy. *Oncotarget* **8**, 30524 (2017).
199. Ho, C. J. H. et al. Multifunctional photosensitizer-based contrast agents for photoacoustic imaging. *Sci. Rep.* **4**, 5342 (2014).
200. Srivatsan, A. et al. Gold nanocage-photosensitizer conjugates for dual-modal image-guided enhanced photodynamic therapy. *Theranostics* **4**, 163–174 (2014).
201. Lin, J. et al. Photosensitizer-loaded gold vesicles with strong plasmonic coupling effect for imaging-guided photothermal/photodynamic therapy. *ACS Nano* **7**, 5320–5329 (2013).
202. Liu, T. et al. Combined photothermal and photodynamic therapy delivered by PEGylated MoS<sub>2</sub> nanosheets. *Nanoscale* **6**, 11219–11225 (2014).
203. Guo, W. et al. Multifunctional theranostic agent of Cu<sub>2</sub>(OH)PO<sub>4</sub> quantum dots for photoacoustic image-guided photothermal/photodynamic combination cancer therapy. *ACS Appl. Mater. Interfaces* **9**, 9348–9358 (2017).
204. Bell, M. A. L., Kuo, N. P., Song, D. Y., Kang, J. U. & Boctor, E. M. *In vivo* visualization of prostate brachytherapy seeds with photoacoustic imaging. *J. Biomed. Opt.* **19**, 126011 (2014).
205. Kuo, N., Kang, H. J., Song, D. Y., Kang, J. U. & Boctor, E. M. Real-time photoacoustic imaging of prostate brachytherapy seeds using a clinical ultrasound system. *J. Biomed. Opt.* **17**, 066005 (2012).
206. Su, J. L., Bouchard, R. R., Karpiouk, A. B., Hazle, J. D. & Emelianov, S. Y. Photoacoustic imaging of prostate brachytherapy seeds. *Biomed. Opt. Express* **2**, 2243–2254 (2011).
207. Das, D., Sharma, A., Rajendran, P. & Pramanik, M. Another decade of photoacoustic imaging. *Phys. Med. Biol.* <https://doi.org/10.1088/1361-6560/abd669> (2021).
208. Yang, W. H., Xu, J., Mu, J. B. & Xie, J. Revision of the concept of anti-angiogenesis and its applications in tumor treatment. *Chronic Dis. Transl. Med.* **3**, 33–40 (2017).
209. Pinker, K. et al. Clinical application of bilateral high temporal and spatial resolution dynamic contrast-enhanced magnetic resonance imaging of the breast at 7 T. *Eur. Radiol.* **24**, 913–920 (2014).
210. Nael, K. et al. High-spatial-resolution contrast-enhanced MR angiography of abdominal arteries with parallel acquisition at 3.0 T: initial experience in 32 patients. *Am. J. Roentgenol.* **187**, W77–W85 (2006).
211. Zhuang, B. et al. *Proc. 2012. IEEE Int. Ultrasonics Symp* 1662–1665 (IEEE, 2012).
212. Pagliari, C. M. et al. Diagnostic quality of 50 and 100  $\mu$ m computed radiography compared with screen-film mammography in operative breast specimens. *Br. J. Radiol.* **85**, 910–916 (2012).
213. Rangayyan, R. M., Nguyen, T. M., Ayres, F. J. & Nandi, A. K. Effect of pixel resolution on texture features of breast masses in mammograms. *J. Digit. Imaging* **23**, 547–553 (2010).
214. Prieto, E. et al. Evaluation of spatial resolution of a PET scanner through the simulation and experimental measurement of the recovery coefficient. *Comput. Biol. Med.* **40**, 75–80 (2010).
215. Weinstein, S. P., Conant, E. F. & Sehgal, C. Technical advances in breast ultrasound imaging. *Semin. Ultrasound CT MR* **27**, 273–283 (2006).
216. Kanal, K. M. et al. ACR–AAPM–SIIM practice guideline for determinants of image quality in digital mammography. *J. Digit. Imaging* **26**, 10–25 (2013).
217. Kruger, R. A. et al. Dedicated 3D photoacoustic breast imaging. *Med. Phys.* **40**, 113301 (2013).
218. Harvey, S. C. et al. An abbreviated protocol for high-risk screening breast MRI saves time and resources. *J. Am. Coll. Radiol.* **13**, 374–380 (2016).
219. Dogan, B. E. et al. American College of Radiology-compliant short protocol breast MRI for high-risk breast cancer screening: a prospective feasibility study. *Am. J. Roentgenol.* **210**, 214–221 (2018).
220. Huppe, A. I. et al. Automated breast ultrasound interpretation times: a reader performance study. *Acad. Radiol.* **25**, 1577–1581 (2018).
221. Bernardi, D. et al. Application of breast tomosynthesis in screening: incremental effect on mammography acquisition and reading time. *Br. J. Radiol.* **85**, E1174–E1178 (2012).
222. Hernandez, T. G. et al. Performance evaluation of a high resolution dedicated breast PET scanner. *Med. Phys.* **43**, 2261 (2016).
223. Fowler, A. M. et al. Measuring glucose uptake in primary invasive breast cancer using simultaneous time-of-flight breast PET/MRI: a method comparison study with prone PET/CT. *Radiol. Imaging Cancer* **3**, e200091 (2021).
224. Zhao, T., Desjardins, A. E., Ourselin, S., Vercauteren, T. & Xia, W. Minimally invasive photoacoustic imaging: current status and future perspectives. *Photoacoustics* **16**, 100146 (2019).
225. Manohar, S. & Razansky, D. Photoacoustics: a historical review. *Adv. Opt. Photonics* **8**, 586–617 (2016).
226. Guo, Z. J., Li, L. & Wang, L. H. V. On the speckle-free nature of photoacoustic tomography. *Med. Phys.* **36**, 4084–4088 (2009).
227. Lin, J. C. Microwave thermoacoustic tomographic (MTT) imaging. *Phys. Med. Biol.* <https://doi.org/10.1088/1361-6560/abf954> (2021).

228. Yan, A. et al. Microwave-induced thermoacoustic tomography through an adult human skull. *Med. Phys.* **46**, 1793–1797 (2019).
229. Ji, Z., Fu, Y. & Yang, S. H. Microwave-induced thermoacoustic imaging for early breast cancer detection. *J. Innov. Opt. Heal. Sci.* **6**, 1350001 (2013).
230. Ku, G. & Wang, L. H. V. Scanning microwave-induced thermoacoustic tomography: signal, resolution, and contrast. *Med. Phys.* **28**, 4–10 (2001).
231. Ku, G. et al. Thermoacoustic and photoacoustic tomography of thick biological tissues toward breast imaging. *Technol. Cancer Res. Treat.* **4**, 559–565 (2005).
232. Liang, B. Y. et al. Acoustic impact of the human skull on transcranial photoacoustic imaging. *Biomed. Opt. Express* **12**, 1512–1528 (2021).
233. Na, S. et al. Transcranial photoacoustic computed tomography based on a layered back-projection method. *Photoacoustics* **20**, 100213 (2020).
234. Mohammadi, L., Behnam, H., Tavakkoli, J. & Avanaki, K. Skull acoustic aberration correction in photoacoustic microscopy using a vector space similarity model: a proof-of-concept simulation study. *Biomed. Opt. Express* **11**, 5542–5556 (2020).
235. Mitsuhashi, K., Wang, L. H. V. & Anastasio, M. A. in *Proceedings of SPIE. Vol. 9323: Photons Plus Ultrasound: Imaging and Sensing 2015* (eds Oraevsky, A. A. & Wang, L. V.) 9323 3B (SPIE, 2015).
236. Hosseinaee, Z., Le, M., Bell, K. & Reza, P. H. Towards non-contact photoacoustic imaging [review]. *Photoacoustics* **20**, 100207 (2020).
237. Bell, K. et al. Reflection-mode virtual histology using photoacoustic remote sensing microscopy. *Sci. Rep.* **10**, 19121 (2020).
238. Cox, B., Laufer, J. G., Arridge, S. R. & Beard, P. C. Quantitative spectroscopic photoacoustic imaging: a review. *J. Biomed. Opt.* **17**, 061202 (2012).
239. Tzoumas, S. et al. Eigenspectra optoacoustic tomography achieves quantitative blood oxygenation imaging deep in tissues. *Nat. Commun.* **7**, 12121 (2016).
240. Bauer, A. Q., Nothdurft, R. E., Erpelding, T. N., Wang, L. H. V. & Culver, J. P. Quantitative photoacoustic imaging: correcting for heterogeneous light fluence distributions using diffuse optical tomography. *J. Biomed. Opt.* **16**, 096016 (2011).
241. Kirillin, M., Perekatova, V., Turchin, I. & Subochev, P. Fluence compensation in raster-scan optoacoustic angiography. *Photoacoustics* **8**, 59–67 (2017).
242. Jeng, G. S. et al. Real-time interleaved spectroscopic photoacoustic and ultrasound (PAUS) scanning with simultaneous fluence compensation and motion correction. *Nat. Commun.* **12**, 716 (2021).
243. Manwar, R., Kratkiewicz, K. & Avanaki, K. Overview of ultrasound detection technologies for photoacoustic imaging. *Micromachines* **11**, 692 (2020).
244. Na, S. & Wang, L. H. V. Photoacoustic computed tomography for functional human brain imaging [invited]. *Biomed. Opt. Express* **12**, 4056–4083 (2021).
245. Monchalin, J.-P. Optical detection of ultrasound. *IEEE Trans. UFFC* **33**, 485–499 (1986).
246. Wang, K., Su, R., Oraevsky, A. A. & Anastasio, M. A. Investigation of iterative image reconstruction in three-dimensional optoacoustic tomography. *Phys. Med. Biol.* **57**, 5399–5423 (2012).
247. Hauptmann, A. & Cox, B. Deep learning in photoacoustic tomography: current approaches and future directions. *J. Biomed. Opt.* **25**, 112903 (2020).
248. Davoudi, N., Dean-Ben, X. L. & Razansky, D. Deep learning optoacoustic tomography with sparse data. *Nat. Mach. Intell.* **1**, 453–460 (2019).
249. Bohndiek, S. et al. in *Proceedings of SPIE. Vol. 10878: Photons Plus Ultrasound: Imaging and Sensing 2019* (eds Oraevsky, A. A. & Wang, L. V.) 10878 1N (SPIE, 2019).
250. IEEE International Committee on Electromagnetic Safety (SCC39). IEEE standard for safety levels with respect to human exposure to radio frequency electromagnetic fields, 3 kHz to 300 GHz. IEEE Std C95.1 (IEEE, 2005).

### Acknowledgements

The authors thank R. Cao for useful discussions. The authors are also grateful to J. Ballard, D. Garrett and J. Olick-Gibson for close reading of the paper.

### Author contributions

Both authors made substantial contributions to all aspects of the preparation of this manuscript.

### Competing interests

L.V.W. has a financial interest in Microphotoacoustics, Inc., CalPACT, LLC and Union Photoacoustic Technologies, Ltd., which, however, did not support this work. L.L. declares no competing interests.

### Peer review information

*Nature Reviews Clinical Oncology* thanks the anonymous reviewer(s) for their contribution to the peer review of this work.

### Publisher's note

Springer Nature remains neutral with regard to jurisdictional claims in published maps and institutional affiliations.

### Supplementary information

The online version contains supplementary material available at <https://doi.org/10.1038/s41571-022-00615-3>.

© Springer Nature Limited 2022